WAVE OPTICS SIMULATION OF OPTICALLY AUGMENTED RETROREFLECTIONS FOR MONONSTATIC/BISTATIC DETECTION

THESIS

John J. Tatar III, Captain, USAF

AFIT/GEO/ENP/09-M03

DEPARTMENT OF THE AIR FORCE
AIR UNIVERSITY

AIR FORCE INSTITUTE OF TECHNOLOGY

Wright-Patterson Air Force Base, Ohio

AFIT/GEO/ENP/09-M03

WAVE OPTICS SIMULATION OF OPTICALLY AUGMENTED
RETROREFLECTIONS FOR MONONSTATIC/BISTATIC DETECTION

THESIS

Presented to the Faculty

Department of Engineering Physics

Graduate School of Engineering and Management

Air Force Institute of Technology

Air University

Air Education and Training Command

In Partial Fulfillment of the Requirements for the

Degree of Master of Science in Electrical Engineering

John J. Tatar III, BS
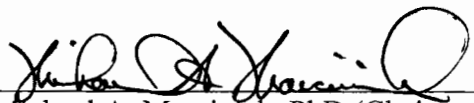
Captain, USAF

March 2009

AFIT/GEO/ENP/09-M03

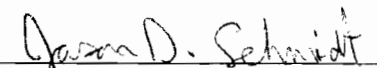# WAVE OPTICS SIMULATION OF OPTICALLY AUGMENTED RETROREFLECTIONS FOR MONONSTATIC/BISTATIC DETECTION

John J. Tatar III, BS

Captain, USAF

Approved:
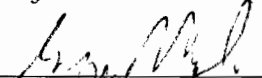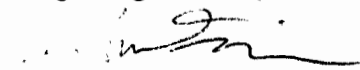
_____
Michael A. Marciniak, PhD (Chairman)

20 Mar 09
_____
Date

_____
Maj Jason Schmidt (Member)

18 Mar 09
_____
Date

_____
George Vogel, PhD (Member)

13 Mar 09
_____
Date

_____
Mr. Shawn Davidson (Member)

19 MAR 09
_____
Date

Abstract

Optical devices interrogated with a laser in the appropriate band can exhibit strong, deterministic reflections of the incident beam. This characteristic could be exploited for optical target detection and identification. The distribution of reflected power is strongly dependent on the geometry of the interrogation scenario, atmospheric conditions, and the cross section of the target optical device. Previous work on laser interrogation systems in this area has focused on analytic models or testing. To the best of my knowledge, I am presenting for the first time an approach to predict reflected power for a variety of interrogation configurations, targets, and propagation conditions using numeric simulation based on wave optics. Numeric simulation has a cost advantage over laboratory and field experiments and avoids the limiting complexity of analytic models. Moreover, results demonstrate that reflected power can be predicted within error with an appropriately characterized. Simulations were prepared in MATLAB and run for interrogation scenarios using a simple retro-reflector (corner cube) and a surrogate complex optical system (lens-mirror) target. Laboratory and field experiments were conducted for simulation validation in the absence and presence of atmospheric turbulence with a focus on bistatic receiver configurations. Two interrogation wavelengths, 1064nm and 4636nm, were used. Targets used in this experiment were modeled in simulation by measuring or estimating their deviation from a perfectly flat reflector and applying the corresponding Zernike mode phase aberrations to the simulated pupil. Strengths and limitations of the simulation environment are addressed.

Acknowledgments

Table of Contents

List of Figures

Figure

List of Tables

WAVE OPTICS SIMULATION OF OPTICALLY AUGMENTED RETROREFLECTIONS FOR MONONSTATIC/BISTATIC DETECTION

I. Introduction

A. Background

Electro optical (EO) devices have become pervasive on today's battlefield. Presence of an optical device typically means observation by friend or foe. It is therefore of great tactical interest to be able to detect, identify, and defeat if necessary, optical devices present on the battlefield. The common approach to this problem is to use lasers in the passband of the optical device of interest and measure the reflection with photonic detectors. The nomenclature for such a system would be a laser interrogation system. When optical devices are interrogated with a laser in the appropriate band, they can exhibit strong, deterministic reflections of the incident beam; a phenomenon known as optically augmented (OA) reflection. OA reflections tend to be retroreflections in that they return to the receiver on the same path as the source. The factor that describes how well an optical device exhibits OA is the optical cross section (OCS). Substantial challenges exist in developing a laser interrogation system which returns enough data to provide detection and identification of optical systems. The optical devices a laser interrogation system is interested in detecting are being operated at ranges from 500m to 3km, and the extent of the optics is small in relation to that distance, thereby limiting the incident flux that can be practically applied. In addition, because the laser interrogation system would need to be used in a tactical environment, atmospheric turbulence will be present to degrade the observable reflection from its diffraction limited form. Lastly, it is

1

unknown if substantial information exists from the reflection to determine target type. It is because of these challenges that research in this area is of importance to the design and implementation of an optical laser interrogation system. Previous research in evaluating optical devices through laser interrogation has focused on laboratory and field experimentation, as well as prediction using analytic predictive models with a heavy emphasis on monostatic or on-axis returns. There is a desire to find an approach to predictive modeling that accounts for characteristics of complex targets and effects of atmospheric conditions, as well as information about the entire reflected power distribution in the receiver plane. `

B. Problem Statement

The intent of this research is to show that numeric wave optics can be used to develop a simulation which provides reflected power distributions from retroreflecting targets in the presence of atmospheric turbulence. The focus will be on characterizing the bistatic or off-axis distribution since on-axis results are well known and can be predicted analytically. The impact of bistatic measurements as well as atmospheric turbulence on the OCS of a target will be discussed.

C. Methodology

This research will use a two-tiered approach to address the problem as stated above. The first tier will be writing a simulation and conducting experiments for two target types and two interrogation wavelengths. The second tier will be a comparison of simulation results with both laboratory and field experiments. The comparison will assess the ability of the simulation to predict the results of a laser interrogation scenario

2

under experimental conditions. The targets used will be simple retroreflecting targets: a corner cube with a one-inch circular aperture and a one-inch circular lens focused to a one inch mirror. The lens-reflector target will serve to model an OA target akin to a more complex EO system. Two interrogation wavelengths will be used, one in the near infrared (NIR) at 1064nm and one in the mid-wave infrared (MWIR) at 4636nm. It will be shown that the NIR is more susceptible to atmospheric turbulence while the MWIR is less affected and provides for a good comparison in field measurements.

D. Preview

Chapter 2 of this thesis provides a look at previous research in the area of OA and related fields, and discusses how the research of this thesis contributes to that limited body of research.

Chapter 3 presents the technical background necessary for the execution and understanding of this research. It includes the approach taken in writing the simulation and the setup of both laboratory and field experiments.

Chapter 4 reports and discusses the results from experiments and demonstrates how well the simulation is able to predict those results. It also provides information specific to implementation and execution of the simulation and experiments.

Chapter 5 offers the conclusions drawn from this research and includes a discussion of future work which could contribute to or improve upon the research presented.

II. Literature Review

A. Chapter Overview

The purpose of this chapter is to present previous research and analysis of theoretic, simulated, and measured properties of optical retroreflection. It should be noted that the laser interrogation system for OA reflections described here is a special case of laser radar, which is widely studied. Specifically, there is not a large quantity of research published which is directly related to OA reflections. There is a series of three works by Abel, Lemery, and Cole from AFIT directly related to OA reflection and laser interrogation which used much of the same equipment and techniques that are used in this research [1,2,3]. There are reports at various classification levels measuring OCS and returned power from optical devices, but they are rooted in analytic models or experiment. There is one OA reflection work which demonstrates how bistatic measurements are an important consideration when interrogating an optical device. It is common to use numeric electromagnetic propagations through turbulence to address a variety of problems in laser radar, medicine, optical communication, astronomy, and other image based sciences. There was no research found in open literature in which the modeling techniques used in this research have ever been applied to the problem presented here. Cole conducted a broad and deep look into the use of the laser range equation in literature for prediction of returned power in turbulence. Cole's dissertation contains excellent references beyond the scope of this work [3].

B. Relevant Research

The approach to the problem presented in this research utilizes electromagnetic wave propagation theory, optical turbulence theory, and tools that are widely used in the fields of astronomy, directed energy, and optical communication. The laser interrogation system investigated in this research is a special case of laser radar where optical retroreflecting targets are of interest. The interrogation occurs under the influence of optical turbulence.

There is an astounding body of research on the subject of characterization of and propagation through optical turbulence including many full text books [4,5]. Analytic treatments of propagation and diffraction from ideal apertures in optical turbulence have been addressed in these texts, as well as in open literature [6,7]. A very important topic to the detection problem while operating in turbulence, especially for horizontal interrogation paths where turbulence can dramatically perturb signals, is scintillation. Scintillation is the random fluctuations in received power for a given detecting scheme that is directly attributed to optical turbulence. Scintillation has been observed experimentally and has been characterized analytically many times [8,9]. Only the Andrews and Phillips text considered OA, using a variety of limiting approximations to arrive at tractable analytic solutions [4].

Another concept used in this research which is widely studied and utilized is the use of computers and numeric methods to solve propagation through turbulence using a thin phase screen [10]. The use of angular spectrum propagation, which is discussed further in Chapter 3, has been shown to be an effective way to compute propagation numerically [11]. There are at least two commercially available software packages which

provide users the tools to make propagation computations through turbulence: WaveTrain

by MZA Associates Corporation and the MATLAB toolboxes *Waveprop*/*AOTools* by

The Optical Sciences Company (tOSC); both were used in this research. Both programs

are designed to implement adaptive optics and beam control systems. A study done by

the Georgia Tech Research Institute (GTRI) utilized numeric methods and *Waveprop* to

model laser radar experiments [12]. The purpose was to demonstrate laser radar as a

means to measure atmospheric turbulence in the same way a commercial scintillometer

does by measuring log-amplitude fluctuations in received power. Although the

simulations conducted by GTRI were similar in some respects to those conducted in this

research, it was a fundamentally different problem in that no OA was involved and only

fluctuations in received power were of interest. It does, however, reinforce the validity of

the methods used in this research.

There is significantly less published work available on propagation problems

dealing with OA, but there are several important sources. An analytic treatment of

retroreflection was accomplished by Lutomirski and Zhengfang for a corner cube

retroreflector [13,14]. Both authors, with the addition of Holmes and Andrews and

Phillips, explored the phenomenon of enhanced backscatter [15,4]. Enhanced backscatter

is observed from retroreflecting targets in turbulence as an on-axis peak of returned

power exceeding the vacuum prediction. Enhanced backscatter occurs for a limited set of

conditions related to aperture size and propagation distance, which are not met in any of

the scenarios in this research. Andrews explored the use of different turbulence power

spectrums to derive analytic expressions describing the mutual coherence function (MCF)

of retroreflections [16]. He demonstrated that usage of the modified spectrum (as

6

opposed to the Kolmogorov spectrum) reduces the beam spread caused by turbulence outer scale effects. Outer scale effects cause low frequency aberrations such as tilt so the modified spectrum limits such low frequency aberrations. Outer scale and inner scale were not computed for the experiments in this research; therefore, it would be impractical to use a spectrum other than Kolmogorov (which does not require knowing outer scale and inner scale). Also, experimental results do not demonstrate a beam spread less than that predicted by Kolmogorov turbulence, a key finding of Andrews' work, suggesting that Kolmogorov turbulence is adequate for this work. Many of the analytic treatments of retroreflection, including those found in the Andrews and Phillips text, use Gaussian models of the retroreflector. This approximation yields tractable analytic results but is not instructive when seeking solutions for real targets. In addition, most of the analytic treatments are concerned with monostatic, or on-axis, detection. The work in open literature related to bistatic, or off-axis, detection is even less prevalent. Lading demonstrated lidar performance in turbulence for both monostatic and bistatic configurations, but not for a retroreflecting or OA target [17]. While his findings showed that bistatic channels are more sensitive to turbulence, his experiments were conducted in a lab with uncharacterized turbulence.

A central topic to OA is that of OCS. Researchers interested in tracking orbiting satellites from the ground have done research measuring OCS in turbulence or predicting returned power based on known OCS [18,19]. Riker used analytic calculations to predict returned power and to measure OCS of an orbiting satellite. Lukesh used monte-carlo simulations to measure the probability of detection but it was not wave optics based. Neither work studied bistatic returns.

The first work specific to OA, in general, was done by Quest Research Corporation and Raytheon with OCS derivations and standards for measurement of OCS [20,21]. These documents are still used today by the Air Force Research Laboratory, Materials and Manufacturing Directorate, Hardened Materials Branch (AFRL/RXPJ) as standards for measurement of OCS. Techniques similar to those of AFRL/RXPJ are also used by the White Sands Missile Test Range. These documents do not provide OCS measurement data but do provide the theoretic equations necessary to compute OCS. The Quest and Raytheon papers also introduce the concept of total OCS (TOCS) and differential OCS (DOCS). The concept of OCS is explored in detail in Chapter 3.

Despite theoretic derivations of OCS and standards for OCS measurement, when the OCS of real optics was measured, the theoretic OCS equations over-predicted the measured OCS [1]. Abel's work confirmed the suspicion that the reduction in measured OCS was due to the aberrations present in real targets. Abel used a wave optics approach to show the OCS reduction from aberrations, although he did not simulate an entire laser interrogation scenario and his results were for OCS in vacuum. This research did show that wave optics could be a viable tool for OCS analysis.

The laser range equation, which is introduced in detail in Chapter 3, is the most popular way to predict returned power from a laser reflection, assuming the target is uniformly illuminated and its cross section is known [22]. Lemery performed field experiments attempting to show the validity of the laser range equation to OA targets [2]. Lemery measured the OCS of a corner cube and lens-reflector target. Her work showed that the laser range equation worked well at long ranges although she did not show why.

She also showed that there was a large error in the received power measurement in the field.

Lemery's findings motivated the work of Cole to examine the applicability of the laser range equation for a wider variety of experimental conditions. Cole derived an analytic correction factor for the laser range equation for an OA reflection under the conditions of monostatic detection [23,24,25,3]. Cole's approach used ray matrix optics in conjunction with the statistical beam transformations due to turbulence as presented by Andrews and Phillips [4]. He showed agreement at several different wavelengths and different relative turbulence strengths for a corner cube and lens-reflector target. The primary disadvantage to Cole's approach is that it only described returned power for a monostatic system. It is also unclear how applicable the correction terms would be to more complex optical systems.

One paper that addresses OA reflections directly is by Chiu [26]. Chiu's work looked at retroreflection from Germanium lens IR cameras with the purpose of finding the bistatic angle to detect military IR systems on the battlefield. Chiu's experiment makes the laser incident on the lens at various transverse locations, adjusts the focus of the lens/detector system, and also tilts the lens with respect to the optical axis. By varying those parameters, the location of the received retroreflection focal spot is mapped out. Chiu's experiments showed how varying the focal length and angle of incidence on the lens can alter the power and observed position of the retroreflection. He verified the expected result for which the highest reflected power occurs is a lens that is most closely focused at the reflecting plane. In the field, it is unlikely that an optical device would be interrogated on boresight, so the results offer an argument for a bistatic detection scheme

when interrogating focusing optics. Because Chiu's experiment was performed in the laboratory, the laser source used to interrogate the optical device was very narrow and did not fill the optic. Therefore, the results provide little information about the performance of a practical laser interrogation system which would make a source with such small extent impractical from both a scanning source and detection standpoint. Also, Chiu did not examine the effects of turbulence present on the reflection.

C. Summary

While there is a large body of information dedicated to the study of propagation in turbulence, using wave optics to demonstrate monostatic and bistatic detection of OA targets is unique. Most of the work in detecting retroreflecting targets in turbulence has focused on deriving analytic solutions with some experimental data collection. Also, laser interrogation geometry focused on monostatic detection. While numeric wave optics simulations have been used in other fields, the detection of OA reflections is not one of them. It is with the findings of this literature review that the work presented in this thesis presents an original contribution to the characterization and detection of OA targets in turbulence.

III. Background and Methodology

A. Chapter Overview

The theory and background required to conduct the experiments will be presented as well as the approach and methodology for experiments and simulations. There are essentially two different approaches to determine received power for a laser interrogation system, radiometry and wave optics. Both methods will be used to derive expressions for returned power and show how, when used together, can yield solutions for monostatic and bistatic returns. The concept of propagation through atmospheric turbulence will be introduced. It will be shown how numeric simulation can be used to solve the equations of optical propagation for the laser interrogation system. Lastly, to validate the simulation, the setup of field experiments will be presented.

B. Background

a. Radiometry and the Laser Range Equation

The power received from a laser reflecting from a target can be calculated from the laser range equation given by [22]

$$P_{received} = \frac{P_{laser} A_{rec}}{\Omega_{laser} R^4} \sigma_T \tau_a^2 \tau_{Tx} \tau_{rec}, \qquad (1)$$

where P is power, A_{rec} is the area of the receiver aperture, Ω_{laser} is the solid angle the source laser beam transmits into assuming the target plane is uniformly illuminated, R is the range to the target, σ_T is the optical cross section (OCS) of the target, and τ_a, τ_{Tx}, and τ_{rec} account for losses due to the atmosphere, transmitter, and receiver, respectively. The conditions of the laser range equation's applicability are revealed through its derivation.

11

The general laser interrogation scenario can be seen in Figure 1, where the transmitter

and receiver are located in a plane some distance from a target. Although this derivation

has been done many times in literature [22], it is useful to recreate the derivation

considering the most basic monostatic configuration where the transmitter and receiver

optics are collocated and boresighted with the target so that the θ angles in Figure 1 are

all zero. All the targets in this research will be interrogated at boresight. Using

principles from radiometry, the laser range equation can be derived [27]. The derivative

of laser power at the target plane with respect to target area gives the irradiance at the

target as shown by

$$E_T = \frac{dP_{laser}}{dA_{laser}} \tau_a \tau_{Tx}, \tag{2}$$

where A_{laser} is the area into which the source emits. If the target plane is uniformly

illuminated, Equation (2) can be rewritten as

$$E_T = \frac{P_{laser}}{A_{laser}} \tau_a \tau_{Tx}. \tag{3}$$

Since uniform illumination is assumed over the target aperture, A_{laser} can be rewritten in

terms of the solid angle subtended by the area of the uniform field at the target plane.

Equation (3) becomes

$$E_T = \frac{P_{laser}}{\Omega_{laser} R^2} \tau_a \tau_{Tx}. \tag{4}$$

The power reflected from the target is a function of the incident irradiance, the target

area, and the reflectance of the target, and can be written as

$$P_T = \rho \int_{Target} E_T dA_T, \tag{5}$$
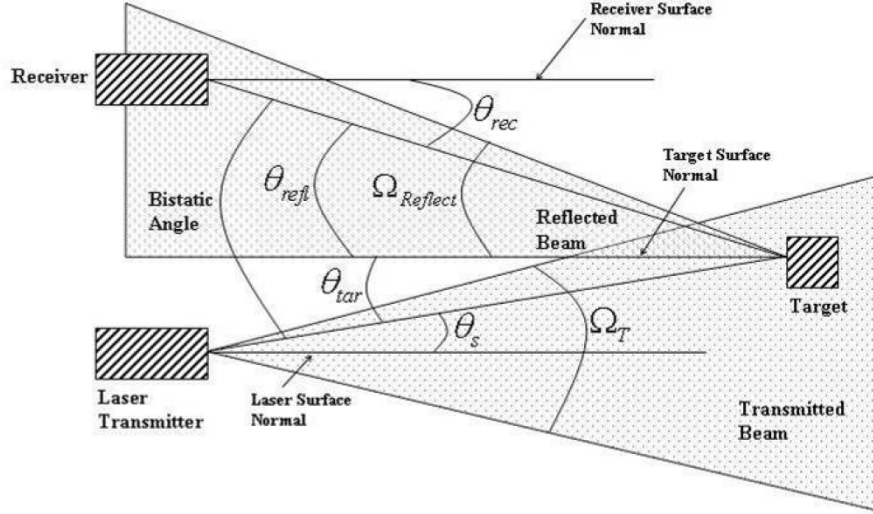
Figure 1. Basic geometry of a nonspecific laser interrogation or laser radar system

where ρ is the reflectance of the target and P_T is the reflected power. Again, for the case of a uniformly illuminated target,

$$P_T = \rho E_T A_T. \tag{6}$$

To find the quantity of ultimate interest, received power (P_{rec}), the irradiance at the receiver is integrated over the area of the receiver as shown by

$$P_{rec} = \tau_a \tau_{rec} \int_{receiver} E_{rec} dA_{rec}. \tag{7}$$

Assuming uniform illumination of the receiver, Equation (7) can be written as

$$P_{rec} = \tau_a \tau_{rec} E_{rec} A_{rec}. \tag{8}$$

It is recognized that for uniform illumination at the receiver plane,

$$E_{rec} = \frac{P_T}{A_{refl}}, \tag{9}$$

where A_{refl} is the area into which the reflection emits. Substituting Equation (4) into (6), (6) into (9), and (9) into (8) yields,

$$P_{rec} = \frac{P_{laser} A_{rec} A_T}{\Omega_{laser} R^2 A_{refl}} \rho \tau_a^2 \tau_{rec} \tau_{Tx}. \tag{10}$$

Rewriting A_{refl} in terms of the solid angle subtended by the uniform field at the receiver, as was done for A_{laser}, gives

$$P_{rec} = \frac{P_{laser} A_{rec}}{\Omega_{laser} R^2 R^2} \frac{\rho A_T}{\Omega_T} \tau_a^2 \tau_{rec} \tau_{Tx}. \tag{11}$$

which allows for the introduction of the OCS term (σ) which will be the subject of an entire subsequent section. For this derivation, OCS is defined as

$$\sigma = \frac{\rho A_T}{\Omega_T}, \tag{12}$$

which completes the derivation of the laser range equation as presented in Equation (1).

It is important to note that this derivation is only valid when the target and receiver planes are uniformly illuminated. Because of the divergence angle of practical laser sources as well as those used in the experiments herein, uniform illumination of the target is a reasonable assumption under turbulence free conditions. For the case where the receiver aperture is not uniformly illuminated, the derivation of the laser range equation changes and the OCS term becomes largely dependent on the target. The OCS is the most important consideration when deriving the laser range equation for the bistatic detection of optical reflections.

b. Optical Cross Section (OCS)

The optical cross section is a characteristic of an optical target which describes the intensity of the reflection per target irradiance. The general form of optical cross section is given by (OCS Primer) as

$$\sigma = \frac{I_T}{E_T},\qquad (13)$$

where σ is the OCS, I_T is the reflected intensity from the target in W/Sr, and E_T is the irradiance of the target in W/m^2. A distinction between a total optical cross section (TOCS) and a differential optical cross section (DOCS) is made in the literature [20], [21], [24]. TOCS describes the calculated OCS when all reflected power is collected and DOCS describes the calculated OCS when some portion of the reflected power is captured. The published derivations for TOCS and DOCS (specifically the peak DOCS) are typically for limiting cases and care must be taken when using the reported equations. Peak DOCS describes the scenario when the receiver is illuminated by the peak of the target reflection where the receiver is much smaller than the extent of the reflected power distribution, resulting in uniform illumination of the receiver aperture. The equation presented by Arenberg to determine when TOCS or peak DOCS is applicable to a particular interrogation scenario is [21]

$$Q = \frac{z\lambda}{R_{rec} R_{tar}},\qquad (14)$$

where z is the separation between target and receiver and R_{rec} and R_{tar} are the receiver and target radii, respectively. When $Q \ll 1$, the TOCS derivation can be used. When $Q \gg 1$, the peak DOCS derivation can be used. The target and receiver optics used in the experiments of this research were all one inch in diameter and the field experiment test

range was 782m. This yields Q values of 22.48 and 5.16 for the 4636nm and 1064nm interrogation wavelengths, respectively. These values suggest that neither the TOCS or peak DOCS derivations will be applicable to this interrogation scenario and Equation (13) will be the preferred method to derive the OCS of the targets.

The derivation of OCS when diffraction effects are observed by the receiver is a valuable example for this work since diffraction will be a dominant effect for off-axis measurement. The corner cube and lens-reflector targets used are essentially circular apertures, so it is instructive to consider Equation (13) for a boresighted circular aperture. For the experiments in vacuum conducted in this research, the target was always uniformly illuminated. Therefore, the denominator becomes,

$$E_T = \frac{P_T}{A_T}. \tag{14}$$

The numerator term, I_T, is not as straight forward. Depending on the size of the target, size of the receiver, and the distance between the target and receiver, diffraction effects could cause the power distribution at the receiver plane to be non-uniform. In such a scenario,

$$I_T = \rho \frac{dP_T}{d\Omega_T}. \tag{15}$$

Assuming the receiver is sufficiently far from the target to be far-field, the power reflected from a circular aperture can be determined through the use of the Fraunhofer irradiance from a circular aperture. The irradiance at a receiver aperture some distance, z, from a circular aperture of diameter d_T is [28]

$$E_{refl}(r) = P_T \left(\frac{\pi d_T^2}{4\lambda z}\right)^2 \left[2\frac{J_1(kd_T(r-x)/2z)}{kd_T(r-x)/2z}\right]^2, \tag{16}$$

where, $J_1(r)$ is the Bessel function of the first kind, r is a radial distance from the center of the receiver, and because the irradiance pattern is azimuthally symmetric, x is the distance from the origin of the receiver plane to the center of the receiver. To find the power incident on the receiver, Equation (16) must be integrated over the area of the receiver. Thus, the power at a circular receiver is given by

$$P_r = \int_{A_r} E_{refl}(r)dA_r = P_T \left(\frac{\pi d_T^2}{4\lambda z}\right)^2 \int_0^{d_r/2} \int_0^{2\pi} \left[2\frac{J_1(kd_T(r-x)/2z)}{kd_T(r-x)/2z}\right]^2 rdrd\phi, \tag{17}$$

where d_r is the diameter of the receiver aperture and upon simplification,

$$P_r = P_T \frac{\pi^3 d_T^4}{2(\lambda z)^2} \int_0^{d_r/2} \left[\frac{J_1(kd_T(r-x)/2z)}{kd_T(r-x)/2z}\right]^2 rdr. \tag{18}$$

With the total power incident at the receiver known, plugging the solid angle subtended by the receiver into Equation (15) gives

$$I_T = \rho \frac{4z^2}{\pi d_r^2} P_r = \rho P_T \frac{2\pi^2 d_T^4}{\lambda^2 d_r^2} \int_0^{d_r/2} \left[\frac{J_1(kd_T(r-x)/2z)}{kd_T(r-x)/2z}\right]^2 rdr. \tag{19}$$

Therefore, σ for a circular aperture is

$$\sigma = \rho A_T \frac{2\pi^2 d_T^4}{\lambda^2 d_r^2} \int_0^{d_r/2} \left[\frac{J_1(kd_T(r-x)/2z)}{kd_T(r-x)/2z}\right]^2 rdr. \tag{20}$$

While the analytic mathematics to predict returned power for an unaberrated circular aperture is solvable, the expression is complicated and becomes progressively less tractable for more complicated scenarios including aberrated apertures and atmospheric turbulence. Converting continuous mathematical expressions to discrete expressions

solved by a computer is one way to overcome the difficult of solving analytic

expressions. Wave optics expressions solved numerically, which compute EM fields

after propagation, are able to account for more complicated scenarios and avoid solving

for the OCS explicitly; although, OCS can be determined. For that reason, wave optics

and numeric methods is the proposed method to solve for returned power in this research.

c. Optical Propagation in Vacuum

The approach to determining received power in this work was to use wave optics

representations of the electric field. The radiometric and wave optics approaches offer

the same solutions, but the underlying theory is somewhat different. The mathematical

description of optical wave propagation is based on the Huygens-Fresnel integral (the

Rayleigh-Sommerfield integral is derived differently but has the same result). The

Huygens-Fresnel integral was developed by solving Maxwell's equation with boundary

conditions across a finite aperture. It is generally hard to solve directly so

approximations have been developed using series expansions. Specifically, the

propagation of an optical field through vacuum can be computed through use of the

Fresnel approximation to the Huygens-Fresnel integral [28]

$$U(x,y) = \frac{e^{jkz}}{j\lambda z} e^{-\frac{k}{2z}(x^2+y^2)} \iint_{-\infty}^{\infty} U(\xi,\eta) e^{j\frac{k}{2z}(\xi^2+\eta^2)} e^{-\frac{2\pi}{\lambda z}(x\xi+y\eta)} d\xi d\eta, \qquad (21)$$

where x and y are horizontal and vertical coordinates in the plane of observation,

respectively, ξ and η are horizontal and vertical coordinates in the source plane,

respectively, λ is the optical wavelength, k is the wave number, and z is the distance from

the source to the observation plane. The Fresnel approximation is valid for all distances

except those very close to the aperture [28].

18

Another approach equivalent to the Fresnel propagation integral is known as angular spectrum propagation. The angular spectrum propagation operates by decomposing a source field into a weighted sum of plane waves through Fourier decomposition and then sums the contribution and phase shifts of the plane waves after propagation to some observation point to obtain the propagated field. The mathematical form for angular spectrum propagation is most easily represented in compact operator notation as presented by Gooodman[28]. A full description of the operator notation is too extensive too include here but U represents the electric field, $\mathcal{V}$ is a scaling factor, Q is a quadradic phase factor, and $\mathcal{F}$ is a 2D-Fourier transform. The angular spectrum propagation as derived by Schmidt as [29]

$$U(x,y) = Q\left[\frac{m\pm1}{m\Delta z}\right] \mathcal{F}^{-1} \mathcal{V}\left[\mp\frac{1}{m}\right] Q\left[\pm\frac{\Delta z}{\lambda^2 m}\right] \mathcal{F} \, Q\left[\frac{1\pm m}{\Delta z}\right] \mathcal{V}\left[\mp\frac{1}{m}\right] U(\xi,\eta), \quad (22)$$

where m is the ratio of the source plane size to observation plane size. The angular spectrum is popular for use in numeric simulations involving light propagation because of its flexibility in discrete computations.

d. Atmospheric Turbulence

Equations (21) and (22) only describe light propagation in vacuum. When an optical beam is propagated through an inhomogeneous medium such as the atmosphere, Equations (21) and (22) will not adequately predict the field at the observation plane. When propagating optical fields through the atmosphere, random fluctuations in the index of refraction cause the loss of spatial coherence and scintillation in the propagated field. The degree to which the turbulence perturbs the transmitted beam is traditionally classified as belonging to weak, moderate, or strong regimes[4]. The distinction between

19

weak and strong turbulence is important because each regime has its own set of statistical

theories. Most notably, the statistics for weak turbulence are developed using Rytov

theory and may not be applicable to other turbulence strengths. The amount of turbulent

fluctuations are described for optical applications by the index of refraction structure

constant (C_n^2) which typically takes on values between $1X10^{-17}m^{-2/3}$ and

$1X10^{-13}m^{-2/3}$ but can be less than or greater than those values in some scenarios. The

turbulence strength is defined by some strict definitions which are not only a function of

C_n^2 but also a function of the beam being transmitted. Several measures of turbulence

strength have been suggested in the literature. Andrews and Phillips propose that the

Rytov variance (σ_R^2) is used to characterize weak fluctuations for a Gaussian beam wave

when $\sigma_R^2 <1$ and $\sigma_R^2\Lambda^{5/6}<1$, where Λ is a function of the beam diameter at the target (W)

and is given by $2z/(kW^2)$. When those conditions fail, the turbulence is classified as

moderate to strong[4]. Parenti and Sasiela draw a slightly different distinction, where the

weak turbulence is defined by the value of r_0/D where r_0 is the Fried parameter for a

plane wave given by [8]

$$r_0 = \left[0.423k^2 \int_0^z C_n^2(L)dL\right]^{-3/5}, \qquad (23)$$

and D is the transmitting aperture diameter. When a Gaussian beam is being used, D can

be converted to the Gaussian beam waist parameter (W_0) by the relationship $D = 2^{3/2}W_0$. The weak regime is then defined when $W_0/r_0 \ll 1$ and strong when $W_0/r_0 \gg$

1. For example, in the experiments of this work, using the W_0/r_0 criterion for a laser

with a beam diameter of 6.1mm, a constant C_n^2 of $1X10^{-14}m^{-2/3}$, wavelength of

1064nm, and propagation distance of 782m, $W_0/r_0 = 0.419$. This value nearly meets the

criterion for weak turbulence despite propagating close to the ground where the strong regime might be expected.

Yet another description of weak and strong turbulence is the log-amplitude variance which is sometimes called the Rytov number. In general, under conditions of weak turbulence, the probability density function (pdf) of the power measured at a receiver after a turbulent propagation is approximated by the log-normal pdf. If the measured variance of the log-amplitude is less than 0.25, the turbulence the beam propagated through can be considered weak and Rytov theory applies. The Rytov number can be calculated for a turbulent path in simulation.

e. Modeling Atmospheric Turbulence

Optical turbulence can be modeled by a series of thin phase screens calculated to agree with the turbulence statistics of the scenario [4]. These phase screens can be generated for numerical simulation using techniques outlined by Lukin [30]. The *WaveProp* toolbox in MATLAB automatically generates phase screens that obey fluctuation statistics in agreement with derived power spectra. A variety of fluctuation spectra are available in Andrews and Phillips, Chapter 3, which are selected based on the parameters of the turbulent environment, notably inner and outer scale[4]. As light is numerically propagated over a specified propagation distance, it is multiplied by the random phase screens at various points in the propagation path (the number and location of the screens will be considered in the simulation section). The field at the target plane should match turbulent field statistics. The phase screens generated for this work will have spatial frequency content as described by the Kolmogorov power spectral density (PSD) given by [4]

$$\Phi_n(\kappa, z) = 0.033C_n^2(z)\kappa^{-\frac{11}{3}}, \tag{24}$$

where z is the path distance and κ is the spatial wavenumber. In general, the choice of PSD used to generate phase screens is driven by the propagation path being modeled.

To use any of the derived PSDs, the assumption must be made that the atmospheric propagation path is homogeneous and isotropic. The propagation path in this work is horizontal and is at a fixed height of 2.33m from the ground with no obstructions. Experimental data was collected in cold weather when the ground was frozen so convection between the atmosphere and the ground was minimal. Therefore, the assumption that the atmosphere is homogeneous and isotropic was made since ground/atmosphere convection would be the leading cause of losing homogeneity and isotropy. The Kolmogorov PSD is the least sophisticated of the derived turbulence power spectra in that the equation assumes the turbulence experienced has an infinite outer scale and zero inner scale. Other spectra bound the turbulence PSD by including inner and outer scale effects which are analogous to the size limits of the turbulent eddies. Other PSDs saturate for spatial frequencies less than the spatial frequency corresponding to outer scale and attenuate rapidly for spatial frequencies greater than the spatial frequency corresponding to the inner scale. Therefore, to use Kolmogorov statistics for the turbulence model in this simulation, the propagating beam must not be bigger than the outer scale or smaller than the inner scale. The region where scale sizes are smaller than the outer-scale and larger than the inner scale, known as the inertial sub-range, is where Kolmogorov statistics agree with other more complicated PSDs. Inner and outer scale sizes were not measured for the propagation path in this work so some assumptions were made about inner and outer scale size. A common approximation for inner scale size is

that is it half the size of the path height from the ground [4]. For the experiments in this work with a propagation path height of 2.33m, the outer scale can be estimated at 1.17m. Since the target is only 1in, outer scale should not affect the source propagation in the region of interest. In the case of the reflected distribution, the 4636nm distribution will be larger than the 1064nm distribution as predicted by the diffraction limited spot size. The diffraction limited spot size out to the second ring of the distribution (the limit of the measurements taken) for an ideal circular target at 4636nm case would be 0.639m, less than half the size of the predicted outer scale. Inner scale near the ground is typically observed to be between 3mm and 10mm [31]. The smallest dimension of the beam in this work is at the source where the source diameter is 4.49mm and 6.10mm for the 4636nm and 1064nm sources, respectively. While these beam diameters are within the expected range of inner scale and could be slightly smaller than the actual inner scale, the divergence angle of the sources keeps the diameters less than 10mm for less than 1m of propagation. Therefore, the assumption that most turbulence effects encountered will be unaffected by inner and outer scale sizes was made, justifying the use of the Kolmogorov spectra for the propagation path model in this work.

It is useful to discuss the statistical nature of simulations through optical turbulence using random phase screens. This laser interrogation system can be considered a double-passage problem where the source and reflected propagations encounter the same turbulent path [4]. One propagation of the source and reflection through a random draw of turbulent phase screens represents the reflected irradiance over a very short time scale. The simulated reflected power distribution after one round trip through the turbulence can be considered a short-exposure image. A short-exposure

image occurs when the integration time of the imager/detector is short enough that atmospheric effects are frozen in time and do not evolve [5]. When applying a single random draw of some phase screen set to the source propagation and reflection propagation in reverse order, the state of the phase aberrations in the atmospheric path have effectively been frozen for the period of exposure. If the integration time of an imager/detector is long enough so that the freezing of atmospheric effects is not valid, the resulting power distribution is a long-exposure image. Long-exposure images can be obtained by taking the average of many short-exposure images. In other words, to generate a long-exposure reflected power distribution in simulation requires multiple round trips through different random realizations of turbulence. The number of propagations through unique random draws is determined by the number of propagations it takes to achieve desired results and the available computation time.

C. Simulation Methodology

The choice in software for the writing of the laser interrogation simulation was MATLAB and the MATLAB toolboxes *WaveProp* and *AOTools* provided by tOSC. The choice of the *WaveProp* and *AOTools* software packages was made because of prior experience and the built-in functions to do EM propagation in the presence of atmospheric turbulence. This allowed for much of the code to execute the complicated discrete mathematics inherent in the angular spectrum propagation and computation of turbulent phase screens to be pre-validated and implemented modularly. For the purposes of discussion, the simulation can be dissected into three parts: source propagation, target reflection, and reflection propagation and detection.

a. Source Propagation

For a laser interrogation system, lasers of interest will have beams that are approximately Gaussian. While the propagation of a Gaussian beam is well known and simple to execute mathematically, there were several difficulties in using the Gaussian beam profile in this simulation given the parameters of the laser beam sources that were modeled and the requirement to model turbulence. To understand these limitations, two associated subjects must be explored which are critical to successful numeric simulation; the first is minimizing aliasing as a result of the discrete Fourier transform (DFT) inherent in propagation. The second is providing adequate resolution over target and receiver apertures.

It is understood from discrete transform theory that finite size of real signals and finite sampling frequency contribute to the loss of information and perturbation of the continuous signal [28,32]. The conventional way to deal with most real signals which are finite in size is to pad the signal with zeros [32]. In the case of the two-dimensional electric field that is the Gaussian beam, the real part (i.e., magnitude) of the electric field gets infinitesimally small at the edges. Setting the field of view, or grid size, so that a sufficient amount of the nearly zero valued edges are present has a similar effect as zero padding. While increasing the spatial extent of the grid to a size larger than the field of interest works well to minimize the wrap-around aliasing in the magnitude, it is does not work for the imaginary phase because of the quadratic phase present in Fresnel propagation. The phase of the field describes how the field propagates and must also be protected from aliasing over the region of interest. As seen in Equations (21) and (22), a quadratic phase is inherent in the propagation mathematics. A quadratic phase term is

present in the Gaussian beam equation, as well [4]. The quadratic phase means that the

phase grows or decreases unbounded in all directions on the grid. Phase aliasing occurs

when the phase changes faster than 2π between consecutive samples, resulting in the loss

of phase information. Therefore, scenarios where the derivative of the phase is large are

scenarios strongly impacted by phase aliasing. In general, a combination of the electric

field divergence and the propagation distance will cause phases with large derivatives.

At the heart of compensating for aliasing is the grid spacing. The *WaveProp*

documentation recommends that the number of samples in a grid be equal to or greater

than the Fresnel scaling given by [33]

$$N \geq \frac{S(0)S(z)}{\lambda z}, \tag{25}$$

where N sets the number of samples along one side of the grid, λ is the wavelength of the

field, z is the propagation distance, and $S(0)$ and $S(z)$ are the grid sizes in the source and

observation plane, respectively. There is a rigorous method used to determine the grid

sizes and spacings when using angular spectrum propagation that was developed by Coy

and Schmidt [29]. Defining the source and observation plane apertures and satisfying the

constraints given by

$$1. \quad \delta_2 \leq \frac{\lambda z - \delta_1 D_2}{D_1} \tag{26}$$

$$2. \quad N \geq \frac{D_1}{2\delta_1} + \frac{D_2}{2\delta_2} + \frac{\lambda z}{2\delta_1\delta_2}, \tag{27}$$

where D_1 and D_2 are the source and receiver plane aperture diameters, respectively,

and δ_1 and δ_2 are the source and receiver plane grid spacings, respectively, the grid

spacings which avoid aliasing in magnitude can be determined. For this work, D_1 is the

target with a one-inch diameter and D_2 is the receiver plane where the entire reflected

distribution must be captured. Also, for computational efficiency purposes, N should be chosen to be a power of two. By declaring the values of D_1, D_2, and N, constraint 1 can be ignored and constraint 2 can be minimized with respect to δ_1 and δ_2 using a Lagrange multiplier method. This allows for the smallest grid spacing (i.e., highest resolution) possible for a given N in both the source and receiver planes that satisfies the constraints of Equations (26) and (27). Therefore, as long as N is chosen to exceed the value of N given in Equations (21) and (22), aliasing of the magnitude should be avoided in the region of interest. However, the constraints described above do not consider phase aliasing which must be accounted for if warranted. Also, the grid spacings derived by the constraints are valid for vacuum propagation, so larger grid spacings may be necessary to account for beam spread due to turbulence propagation. An important practical point taken from Equations (26) and (27) is that an increase in spatial frequency in one plane means a decrease in the other.

Given the sampling constraints presented and considering the divergence of the laser sources used in this work, modeling the actual Gaussian beam becomes impractical. As shown by constraint 2, the large size of D_2 necessary to model the beam at the target would make N prohibitively large because of the computation time necessary to conduct the propagations. For example, the 4636nm laser has a divergence of 3.42mrad so the $1/e^2$ diameter of the beam at a target 784m away is 5.4m. To put an adequate guard band on such a Gaussian beam would require a grid at least twice as large. With D_2 equal to 10.8m and the target diameter equal to 25.4mm, to put one pixel across the target aperture would require 432 samples on a side. In practice, one pixel will not be adequate, especially since further propagation must take place from the target. Just to put three

pixels across the target would require 2160 pixels or $N=2^{12}$ pixels on a side to get to the

nearest power of two. To avoid the sampling problem with numerically propagating the

Gaussian beam, an alternate approach was used which capitalizes on the divergence of

the source. Since the source is much larger in extent than the target, it can be assumed

(a)

(b)

(c)
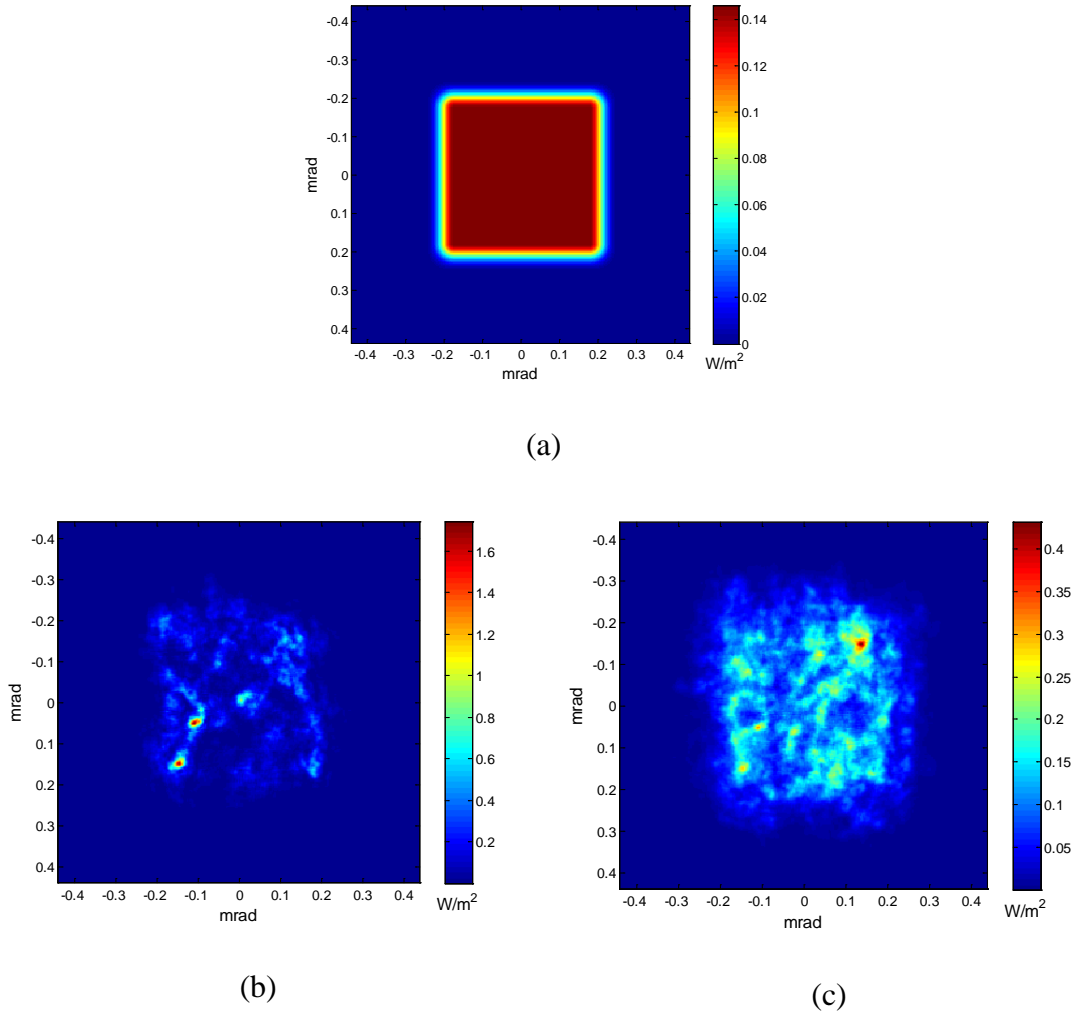
Figure 2. Source irradiance at target distance of 782m. (a) In vacuum. Note spatial filtering at edges to minimize aliasing. (b) After propagation through one random draw (10 phase screens) of turbulence, $C_n^2 = 1.4 \times 10^{-13} \text{m}^{-2/3}$. (c) Average irradiance after 40 propagations through 40 random draws of turbulence.

28

that in vacuum, the irradiance and the phase at the target is uniform. For the sources

employed in this work, this is a reasonable approximation since at 4636nm and 1064nm,

the irradiances at the edge of the targets are 99.9910% and 99.957% of the peak

irradiance at the target, respectively. This approach eliminates the need to use a Gaussian

source in simulation and a source that exhibits equivalent irradiance characteristics at the

target with a smaller spatial extent can be substituted. The choice of source in this work

which met the criteria described was a paraxial portion of a spherical wave. *WaveProp*

has a function *conjsource* which simulates point source propagation for a defined

observation- plane field. To simulate the source, a patch of uniform irradiance was

created, sized to achieve an acceptable number of samples across the target aperture,

spatially filtered to reduce high frequency aliasing, and passed to the function *conjsource*.

For demonstration, the 1064nm irradiance at the target plane after a 782m vacuum

propagation is shown in Figure 2a. Using *WaveProp*, the source can be propagated

through turbulence using the angular spectrum propagation and the random phase screen

techniques as discussed. The 1064nm irradiance at the target plane after a 782m

turbulence propagation through one random draw of phase screens with $C_n^2 =$

$1.4 \times 10^{-13} \mathrm{m}^{-2/3}$ is shown in Figure 2(b). Figure 2(c) shows an average irradiance after

40 propagations. To validate the turbulence propagation to the target, the mutual

correlation function (MCF) of the average turbulent field is computed by performing an

autocorrelation of the field at the target plane. Ideally, the simulated MCF should match

the theoretic MCF for a paraxial spherical wave as given by Andrews and Phillips[4].

Figure 3 shows a vertical slice of the simulated and theoretic two-dimensional MCF with

good agreement.
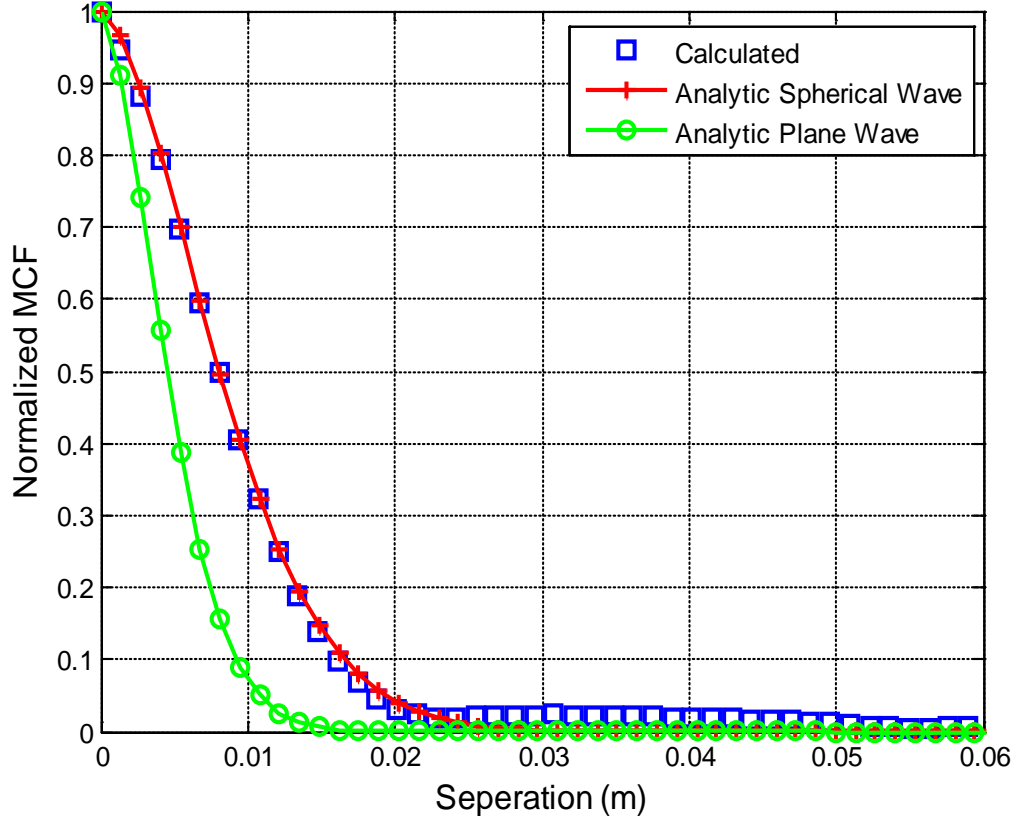
Figure 3. Normalized MCF of the source irradiance after turbulence propagation. Agreement of simulated MCF with analytic expression for a spherical wave in turbulence validates the turbulence model in simulation.

b. Target Reflection

For the simulation to be successful, it must accurately model the effects of reflection from the targets to include power loss due to imperfect reflectivity and transmission of the optical coatings and the aberrations resulting from the imperfect manufacture of the optics. Ideally, at boresight, both the corner cube and lens-reflector target would behave like a perfectly aligned, aberration-free flat mirror with respect to phase, and with a reflectivity of one with respect to amplitude. It should be noted the targets flip the reflected field up/down and left/right due to their geometries. The

reflectivity and transmission of the optics used as a function of wavelength are published by the manufacturer and were used in this work with their associated uncertainty assuming uniform reflectivity and transmission over the extent of the optics. While the aberration tolerances are also published, the actual aberrations present on a particular optic are not known. Interferometery is one method to measure the phase aberrations present on an optical device and was the approach taken here. A practical way to model the phase aberrations of the targets is to apply the effects of the target as they differ from a perfectly aligned and flat reference. Using a Zygo GPI ST interferometer and associated software, the corner cube and lens-reflector targets were compared to the flat reference of the interferometer. The Zygo GPI software reports the phase aberrations in Zernike polynomials which can be used to map the phase aberrations over the target aperture [34]. Phase aberrations are computed in waves and can be scaled proportionally to the interrogation wavelength of interest.

With an accurate representation of the phase aberrations present over the target, multiplying the phase of the aperture by the phase of the incident field will determine how the wavefront of the reflected field transforms during propagation. In addition, the source field incident on the target must be set to zero at all points outside the target aperture so only power reflected from the target is propagated back to the receiver. Figure 4 shows the phase of the target aperture for the corner cube at both 4636nm and 1064nm and the lens-reflector target at 4636nm and 1064nm, respectively. It should be noted that the Zygo measurement technique failed for the lens-reflector targets for reasons that will be discussed in detail in Chapter 4. Figure 4 (c) and (d) show the phase as measured by the Zygo but they were not used in simulation.

31
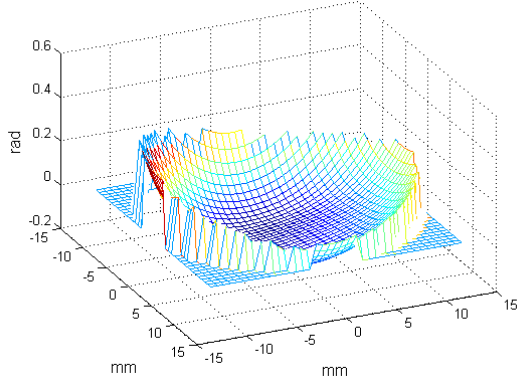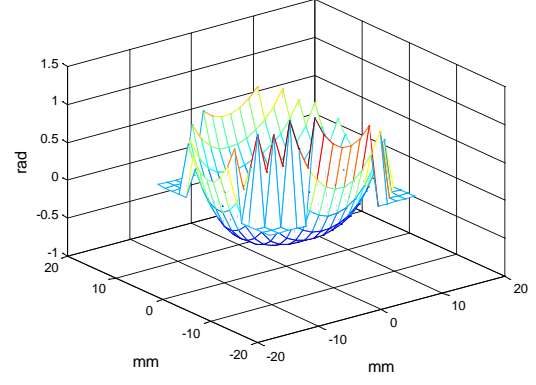
(a) (b)
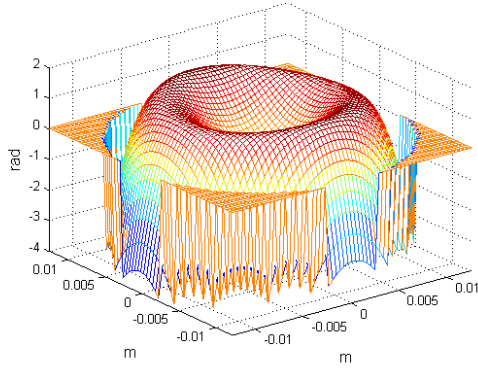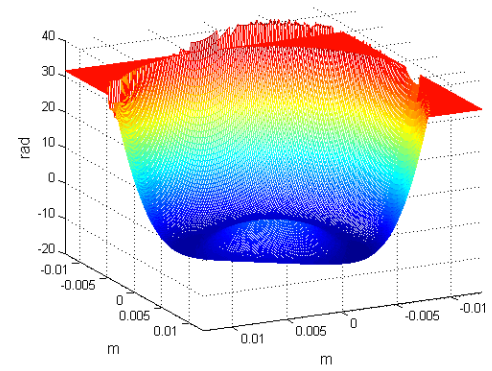
(c) (d)

Figure 4. Aberrated phase of targets as measured by the Zygo interferometer (a) Corner cube at 4636nm (b) Corner cube at 1064nm (c) Lens-reflector at 4636nm (d) Lens-Reflector at 1064nm

c. Reflection Propagation and Detection

With the appropriate irradiance at the target aperture, attenuation due to imperfect reflectivity accounted for, and the phase aberrations over the target aperture applied to the incident field, the electric field can be propagated back to the receiver located in the same plane as the source. In the presence of turbulence, it is physically accurate to return

through the same realization of random turbulent phase screens the source propagation experienced, but in reverse order. This is a reasonable assumption since the speed of light is very fast compared to the time evolution of the turbulence [4]. For reflected field results with minimal aliasing, the sampling constraints that were discussed in the source propagation section must be applied to the reflection propagation. Since the reflected power distribution is spatially larger than the target, the total grid size at the receiver plane must be large enough to accommodate the size of the reflected spot. The radial extent of the reflected spot at the receiver plane can be approximated for input into the sampling constraints by the diffraction limited Airy disk equation for a circular diffracting aperture out to the fourth ring given by [35]

$$r = z \, tan^{-1} \left[2.12 \frac{\lambda}{d/2} \right], \tag{28}$$

where r is the radius of the diffraction limited spot, z is the propagation distance, λ is the wavelength, and d is the diameter of the target aperture. The fourth ring is chosen somewhat arbitrarily so that aliasing in the edges of the power distribution is minimized. Again, a grid spacing must be chosen small enough to allow for sufficient resolution across the receiver aperture. With adequate grid spacings and grid sizes established, propagation back to the receiver can be executed. The resulting electric field at the receiver plane represents the entire reflected power distribution. The magnitude squared of the field provides the irradiance at each pixel. Because the pixels are symmetric in size, the flux through each pixel can be computed by multiplying the irradiance by the area of the pixel (i.e. the pixel size squared). Power will be measured by both laboratory and field measurements so simulated power will be an important quantity. By specifying

the location of a circular pupil representative of the receiver aperture at some position in the receiver plane, the pixel values in the pupil can be summed yielding the total power collected by the receiver.

D. Experimental Methodology

a. Laboratory Measurements OA Reflections in Vacuum

AFRL/RXPJ has designed and implemented an optical bench known as the System Level Characterization Test-bed (SLCT) to measure OCS of a wide variety of optical targets for a wide range of interrogation wavelengths. The SLCT will be used in this work to verify the results of the vacuum simulation. The SLCT has been used only to measure peak DOCS in accordance with the Quest Document [20]. As stated in the OCS section, the peak DOCS is only valid under a specific set of limiting conditions identified by Equation (14). The SLCT has two sides with independent equipment, one for wavelengths below 2000nm (i.e. visible and NIR) and the other for wavelengths above 2000nm (i.e. MWIRIR). The general configuration and operation of both sides is the same.

Figure 5 shows the setup of the MWIRIR side of the SLCT. The essential parts are the laser source which is expanded through a pinhole aperture positioned at the focal point of an off-axis parabolic (OAP) mirror. The source is collimated by the OAP and a target of interest is placed at the center of the collimated field. The target reflection returns through the incident path, and prior to the pinhole, is reflected by a beam splitter into a focal plane array (FPA) detector. Because the detector is positioned at the focal point of
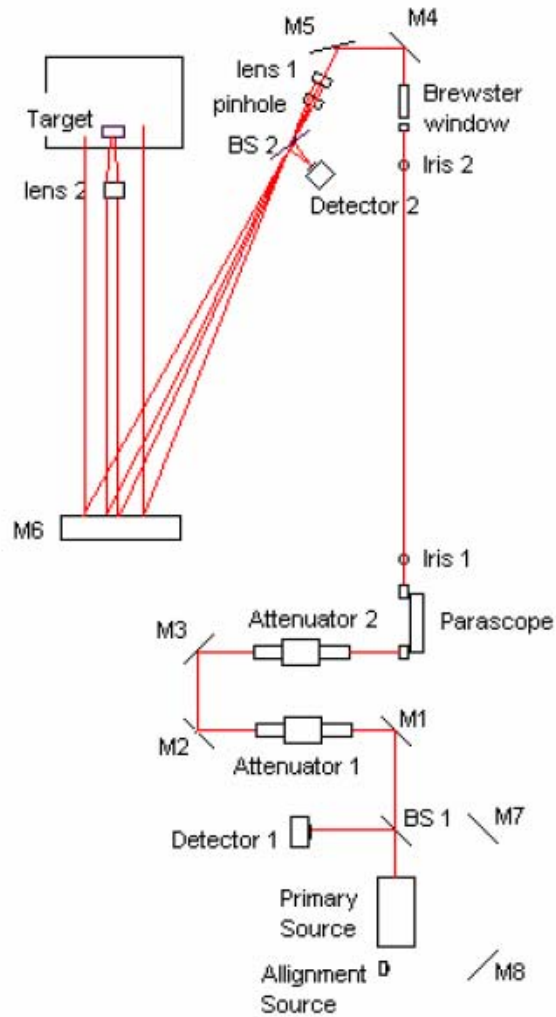
Figure 5. Setup of AFRL/RXPJ SLCT for the measurement of OCS. This schematic is specifically for the MWIRIR side of the bench but the NIR side is nearly identical in configuration.

the OAP, the detector is imaging the scaled Fraunhofer diffraction pattern, or Fourier

transform of the field at the OAP aperture [28]. Vignetting of the reflected field by the

OAP can be ignored for most practical targets because reflections at the OAP will rarely

be larger in extent than the diameter of the OAP. The SLCT sources used to interrogate

the corner cube and lens-reflector targets were a Coherent/DEOS doubled CO_2 MID-IR-2

laser for the 4636nm source and a Crystalaser Nd:YAG laser for the 1064nm source.

Both were operated continuous wave (CW) (quasi CW in the case of the MID-IR-2

because of the fast 100kHz pulse rate) and attenuated to desired power. Targets were

boresighted by finding the orientation to the source which yielded the highest detector

count. FPA detectors were used to capture images of the focused reflections from each

target for comparison with vacuum simulations. The Cohu camera used on the NIR side

of the SLCT was non-uniformity corrected, and both cameras were calibrated to convert

photon count to watts. All measurements were background-subtracted post processing.

Appendix A has a complete listing of equipment used along with specifications.

The Quest document outlines calibration techniques for a measurement apparatus

like the SLCT to compute the peak DOCS [20]. By using a target set of known OCS, a

relationship between the known target cross section and reflected power from that target

can be computed. The SLCT calibration target is a circular optical flat mirror with

circular apertures of varying size. For the monostatic case, where the detector is small

compared to the diffraction pattern, applying those constraints to the OCS derivations

made above, the peak DOCS of a uniformly illuminated circular aperture at boresight is

[21]

$$\sigma = \frac{\rho A_T^2}{\lambda^2},\tag{29}$$

where ρ is the reflectivity of the target, A_T is the area of the target, and λ is the

wavelength of the uniform interrogation source. A calibration curve is computed by

plotting detector counts for a given aperture size vs. theoretical peak DOCS as

determined in Equation (29). A line is fit to the measured count data which produces a

peak OCS gain curve. This curve determines the conversion between detector count and peak OCS. Because a FPA detector is used, the entire focused reflection is captured with multiple pixels over the irradiance distribution. This allows the pixel at the peak to be used as the receiver aperture. This detection scheme meets the requirements for the peak DOCS to be computed with Equation (29) because the peak pixel is uniformly illuminated and the peak of the diffraction pattern is collected. The calibration curve can then be used to predict the peak DOCS of an unknown target when the peak count of the reflection from a target with an unknown peak OCS is measured. The error in the measurement is the fit error of the gain curve to the data.

For interrogation scenarios that do not meet the criteria for using peak DOCS, such as bistatic detection or when the receiver aperture is too large to be uniformly illuminated by the magnitude of the reflection's peak, it may be more appropriate to use Equation (13) directly. To do this on the SLCT, using the previously stated fact that the detector is imaging the scaled Fraunhofer diffraction pattern of the target reflection [28], the size of the measured focused spot can be scaled to the size of a corresponding far-field distribution or vice versa. The scaling factor between the focal plane and the far-field is $U_{far-field} = U_{focus}\frac{z}{f}$, where $U_{far-field}$ and U_{focus} are the field sizes in the far-field and focal plane, respectively, z is the far-field propagation distance, and f is the focal length of the focusing optic. For example, the Cincinnati Electronics FPA camera used on the MWIR side of the SLCT has pixels that are 30µm X 30µm and the OAP which focuses the reflection has a focal length of 2128.37mm. The equivalent size of one pixel at 2km (assuming 2km is a large enough propagation distance for the diffracting aperture and wavelength of interest) is approximately 28.2mm. On the Visible/NIR side,

the Cohu 7712 FPA camera has pixels 7.4µm X 7.4µm in size and the OAP has a

2033.78mm focal length. Because the wavelengths in the visible/NIR are so much

smaller, the central lobe of the focused reflections is on the order of 10 to 20 pixels

square. In order to increase the size of the focused spot on the detector for ease of

measurement, a pair of anti-reflection coated, low aberration lenses are used in front of

the Cohu camera to magnify the spot. The magnification, while not know exactly, is

approximately 3.1 times. Therefore, the equivalent size of one pixel at 2km is

approximately 4.08mm. With the far-field pixel sizes known, the reflected power

distribution can be scaled to the appropriate far-field size for comparison with far-field

simulation. With knowledge of a system-specific receiver size and range to target, the

far-field scaling method allows for the calculation of the reflected solid angle. The

reflected solid angle into which the target emits combined with target size and irradiance

values at the target and FPA allows for any monostatic or bistatic OCS to be calculated,

not just a peak DOCS. The danger in the practical application of the far-field scaling

method is assuming that at long propagation distances a real detector would have

adequate angular resolution to be able to observe a bistatic reflection with the measured

OCS, or make a measurement at all. For the bistatic power measurements described in

the next section, the use of fast collection lenses ensured adequate angular resolution at

the 782m range and bistatic angles of interest.

The SLCT, using the far-field scaling technique above, can be used to validate the

vacuum simulation of the laser interrogation system. The method of scaling the

measured distribution to the far-field has advantages in simulation to modeling the

focusing of the reflected field directly as the increased sampling constraints levied by the

38

focusing quadratic phase factor are avoided. Simulating the propagation of the target reflection in vacuum to a desired far-field distance can be compared with images from the SLCT scaled to the same far-field distance. One addition to the vacuum simulation must be made for comparisons of simulated reflections to those reflections measured on the SLCT. It is important to note that the focused reflection pattern measured on the SLCT is the scaled Fourier transform of the reflection at the OAP aperture. Because the OAP aperture is approximately 3m from the target, the propagation of 3m must be made prior to computing the far-field propagation. This detail is more important for smaller apertures and shorter wavelengths since diffraction effects are more prominent over shorter propagation distances under those conditions.

b. Field Measurements

Field measurements were performed to validate the simulation in the presence of atmospheric turbulence in the same way the measurements made in the laboratory on the SLCT served to validate vacuum simulation results. A laser interrogation system was set up on the Laser Identification (LID) Test Range at Wright-Patterson AFB. In principle, the field experiments were similar to those conducted by Cole, with data collection focusing on the off-axis returns instead of on-axis returns [3]. A pulsed Coherent doubled CO_2 MID-IR-2 laser was used as the 4636nm source and a continuous wave (CW) Crystalaser Nd:YAG laser as the 1064nm source. The 4636nm laser was pulsed and the 1064nm laser was chopped at 1kHz. The corner cube and lens-reflector targets corresponding to the appropriate interrogation wavelength were placed at 782m±2m from

the source and boresighted back to the source. The range to the target was measured with a Newcon Optik LRM 1500 laser range finder. The target was boresighted by adjusting the aspect angle of the target until the detector, in its closest position to the source beam, was showing peak voltage. The photon detector used for the 4636nm interrogation was a liquid nitrogen-cooled Cincinnati Electronics InSb single-element detector. The photon detector used for the 1064nm interrogation was an un-cooled Thor Labs InGaAs single element detector. Both detectors were powered with their voltage signals routed first to a Sanford Research Systems preamplifier and then to a Sanford Research Systems lock-in amplifier. Because of the small size of the detector elements, a one inch lens was used to focus collected radiation onto the detector. Bistatic returns were being measured, so the
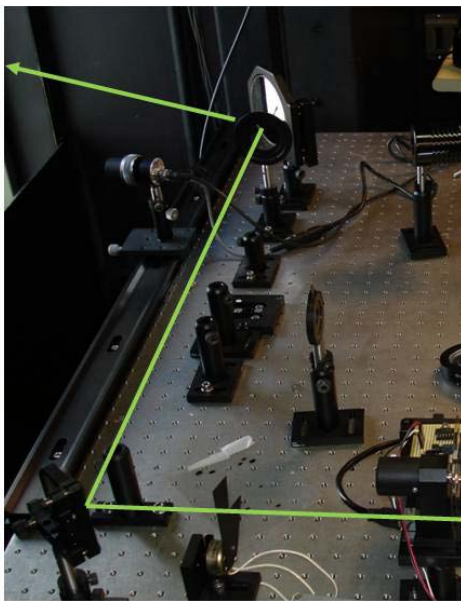
<div align="center">(a)   (b)</div>

Figure 6. Photo of experimental equipment at LID range. (a) Source optics and InGaAs detector set up on bistatic rail. Cartoon of beam drawn in for visualization of source beam path. (b) InSb detector fixture on bistatic rail with collection optics.

detectors were mounted on an optical rail that would allow for measurable lateral movement of the detector relative to the source. Figure 6(a) shows the output mirror and the InGaAs detector in position to its side. The starting position of the detector was set so the edge of the detector aperture was next to the source beam without obstructing the beam. In the case of the 4636nm detector, a significant amount of the detector structure would have obscured several cm of collection area, so a one-inch mirror was used to collect the reflected power and redirect it to the collection lens. Figure 6(b) shows the 4636nm detector apparatus. To characterize atmospheric turbulence conditions, a Scintec Boundary Layer Scintillometer (BLS) 900 measured the one-minute average C_n^2 over the propagation path. Appendix A has a complete listing of equipment information and specifications.

To validate the turbulence interrogation scenario, several quantities needed to be collected experimentally. Received detector voltage, corresponding source laser power, and time the measurement was taken were collected by hand. Because received power is a function of C_n^2, a time stamp for each data point was critical since C_n^2 was being measured, recorded, and time stamped electronically. A three-second time constant was used on the lock-in amplifier from which detector voltage was recorded. The long time constant was necessary to keep measurement fluctuation under control so that data collection by hand was possible. For the 4636nm interrogation, five data points were collected over one minute per detector position. Due to the anticipated size of the reflected power distribution and finite time for data collection, detector position was changed in 2cm intervals. Because measurements were taken by hand, the instability of the MWIR laser power constrained collection to five points in one minute. For the

41

1064nm interrogation, 12 data points were collected over a one minute interval. Since

the reflected power distribution at 1064nm was anticipated to be smaller in extent than

the reflected power distribution at 4636nm, detector position was changed in 1cm

intervals.

E. Summary

The simulation and experiments performed in this research are all grounded in

established theory. Only the most important key points related to radiometry, wave

optics, optical turbulence theory, and optical turbulence simulation were reproduced here.

Wave optics simulations can be designed many different ways. The approach presented

here was intended to highlight some of the more unique points related to the design and

execution of the simulation created for this work. Results of the simulation and

experiments conducted will be presented and analyzed in the next chapter.

IV. Analysis and Results

A. Chapter Overview

The execution of the simulation and experiments discussed in Chapter 3 yielded a tremendous data set of simulation results, laboratory measurements, field measurements, and instrument calibration. That data will be presented in two sets: vacuum simulation compared with laboratory measurements and turbulence simulation compared with field measurements. An attempt will be made to account for any deviations from expected results.

B. Comparison of Vacuum Simulation and Laboratory Measurements

The first target of interest was the corner cube. The SLCT was used at 4636nm to image the corner cube reflection at focus. To simulate the SLCT results, a uniform field was applied to the simulated target. The field at the target is first free-space propagated 3m to simulate the distance between the target and the OAP on the SLCT. The field is then free space propagated 2km to the far-field. The SLCT image can then be scaled to its size at 2km through techniques discussed in Chapter 3. The measured and simulated distributions are all normalized to their peak value. A direct comparison of the actual measured and received power values, as done for the turbulence measurements in the subsequent section, would have been ideal. Failure to collect target irradiance values for the images taken on the SLCT made such a comparison impossible. Figure 7(a) and Figure 7(b) show the scaled SLCT image and the simulated image respectively. The images are normalized to their peak power in watts. Figure 8 shows a horizontal slice
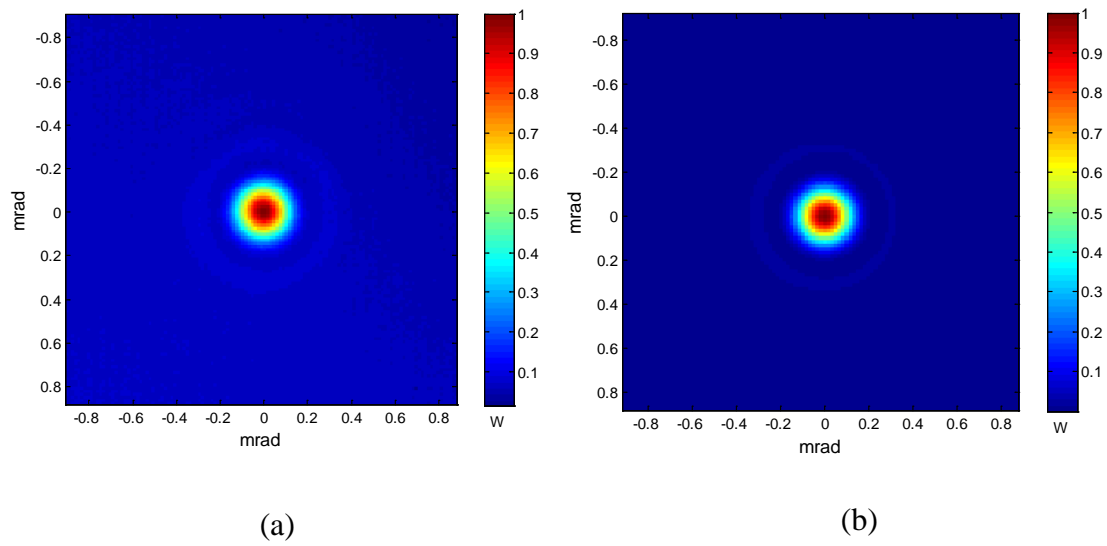
Figure 7. Peak normalized reflected power distributions of the corner cube target interrogated at 4636nm. (a) SLCT data. (b) Simulated data.
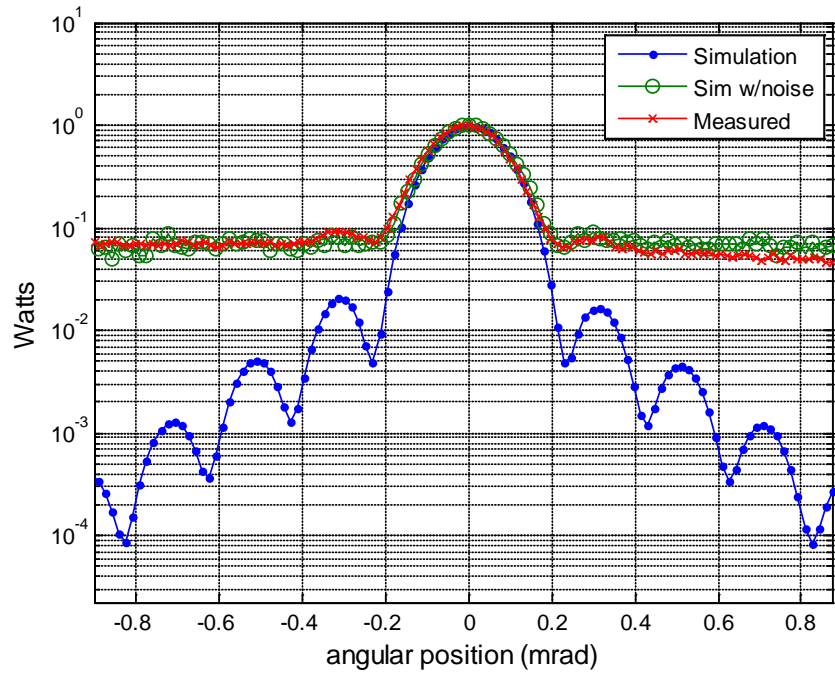
Figure 8. Slice of reflected power distribution from corner cube target interrogated at 4636nm

44

through the center of the SLCT image and the simulated image. As the power

distribution is observed off-axis, the simulated slice shows substantial diffraction effects.

In the SLCT measurement, the noise floor of the FPA detector is 1.5 orders of magnitude

below the peak while the first side lobe of the diffraction pattern is 1.9 orders of

magnitude below the peak. Therefore, nearly all off-axis diffraction effects cannot be

observed. Gaussian random noise was then added to the simulated curve with the same

mean and variance as the measured background frames. Addition of noise demonstrates

good agreement between measured and simulated results even though the added noise is

statistical and may not have the same statistics of the actual detector noise. The noise

floor reported in the SLCT images was substantially higher than expected (~3 orders of

magnitude expected) and was due extra background irradiance not accounted for by

background subtraction. In Chapter 3, it was stated that all images were background

subtracted during post-processing of the images. This means a series of images were

taken to establish the detector counts with no target reflection present. The reflection was

then measured and the average background frame was subtracted from the reflected

power distribution image. This process should help to determine the actual pixel counts

due to the reflection and improve the observed dynamic range of the detector. However,

the background frames taken did not remove the actual amount of background present in

the images. If these images were re-analyzed, the background frames could be scaled to

a higher count so that features with smaller detector counts relative to the peak could be

observed. It is hypothesized that the lapse in time between taking background images and

capturing reflected power distribution images caused the discrepancy between the

magnitude of the background images and the magnitude of the background observed in

the reflected power distribution images. Ideally, background images should have been taken as close to the time as the image was taken as possible to minimize background drift which could occur for environmental conditions as well as fluctuation in detector temperature. Dynamic range greater than three orders of magnitude could have been observed using a technique that takes several images with different integration times. Short integration times could be used to capture high count features while long integration times could be used to capture features with significantly smaller counts. The images could then be combined, removing the saturated features from each image.

Figure 9 and Figure 10 show the same plots for the corner cube target illuminated at 1064nm. Good agreement between measurement and simulation is observed with the addition of noise to the simulated results. The dynamic range of the 1064nm camera is notably better than that of the 4636nm camera due to better background subtraction as observed by the 2.5 orders of magnitude of dynamic range, although it could likely be improved by similar techniques as discussed for the 4636nm images. The left side of the power distribution in Figure 10 shows a small stretch in the curve at -0.07mrad and slight compression of the curve at 0.07mrad. This distortion is due not to target aberrations but to the beam splitter and camera alignment. A beam splitter is used on the SLCT to redirect the reflection to the FPA camera so any deviation of the camera's aspect angle from boresight with respect to the 45° aspect angle of the beam splitter could cause such a distortion. The same effect is shown on the lens-reflector target distribution in Figure 14. Therefore, it is assumed that the beam splitter and camera alignment is responsible for the lateral stretch since the same aberration occurs in both targets at exactly the same point and is unaccounted for by any other measurement.

46

(a)   (b)

Figure 9. Peak normalized reflected power distributions of the corner cube target interrogated at 1064nm. (a) SLCT data. (b) Simulated data.
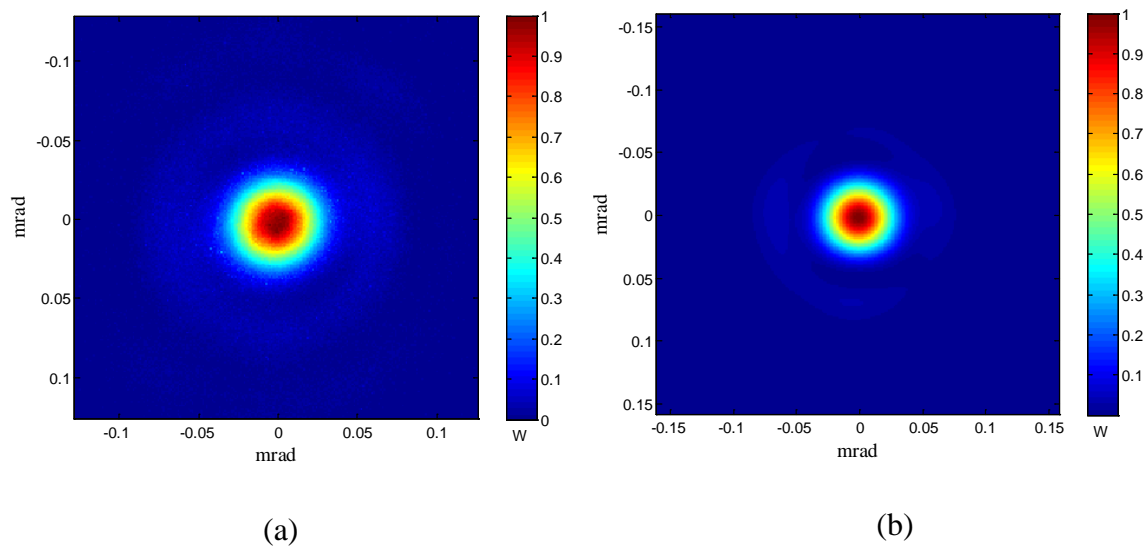

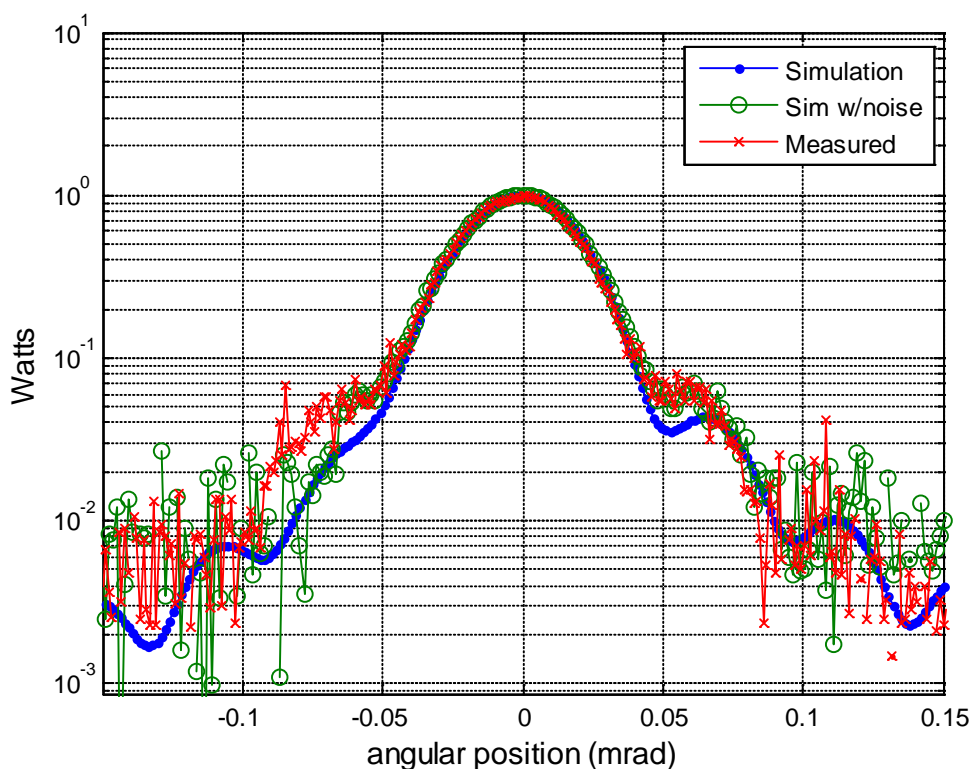**Figure 10. Slice of reflected power distribution from corner cube target interrogated at 1064nm. Note the stretch of the reflected power distribution by the beam splitter of the SLCT at angular positions less then -0.07mrad.**

The assessment of the corner cube targets provides evidence that the use of the interferometer to model target aberrations is a viable method for a corner cube target. It also shows that the vacuum simulation provides an accurate prediction of the free space reflection from the corner cube target. It has been stated that the SLCT has only been used to measure peak DOCS. There is definitely a large enough signal-to-noise ratio at the peak of the focused reflection to be unaffected by the detector noise. If an OCS is to be measured for a scenario which requires the flux measurements off peak, a more careful background subtraction or techniques with variable integration times to increase the dynamic range of the detector should be applied.

The lens-reflector targets can be analyzed the same way as the corner cube target. Figure and Figure 12 show the scaled and normalized SLCT image, the vacuum simulation image, and the horizontal slice of the SLCT image, vacuum simulation, and vacuum simulation with noise at 4636nm. Figure 13 and Figure 14 show the same plots for the 1064nm target. While the 4636nm SLCT measurements and simulation match reasonably well, the agreement for the target at 1064nm is poor, even after the addition of noise. This problem warrants an in depth look at the lens-reflector target and demonstrates that the interferometry method as applied does not provide meaningful results for the reflected phase from the lens-reflector targets.

The Zygo interferometer method does not return reflected phasefront aberrations for the lens-reflector targets because of the chromatic properties of the lenses. The Zygo interferometer uses a 632nm HeNe laser as its source [36] but lens-reflector targets utilized optics which were designed for 4636nm and 1064nm. The targets were identical except for the lens used. Both targets used the same Thor Labs PF10-03-P01 silver

(a)   (b)

Figure 11. Peak normalized reflected power distributions of the lens-reflector target using the interferometer aberrations interrogated at 4636nm. (a) SLCT data. (b) Simulated data. Simulations and measurements agree reasonably well but the 1064nm target suggests the methodology for determining the reflected phase was incorrect.
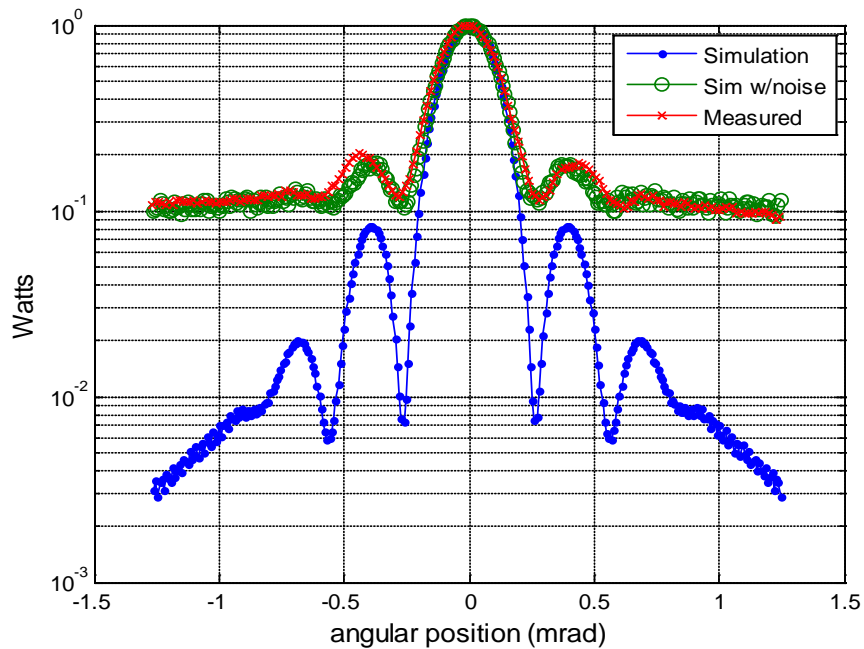
Figure 12. Slice of reflected power distribution from lens-reflector target using the interferometer aberrations interrogated at 4636nm. Simulations and measurements agree reasonably well but the 1064nm target suggests the methodology for determining the reflected phase was incorrect.
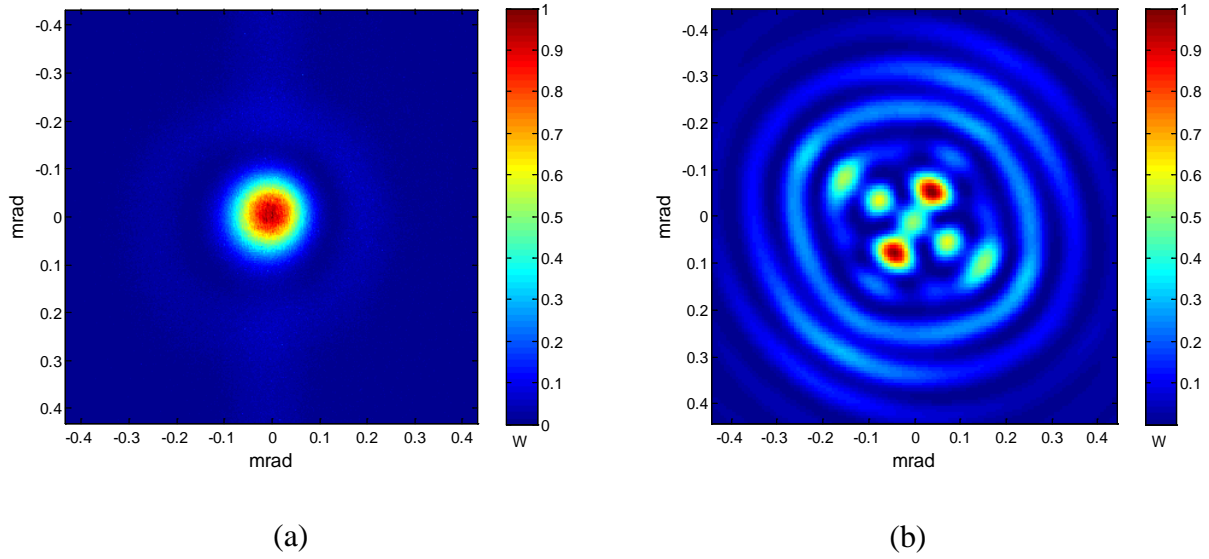
Figure 13. Peak normalized reflected power distributions of the lens-reflector target interrogated at 1064nm. (a) SLCT data. (b) Simulated data. The figures demonstrate the poor agreement of the simulation with measured data.
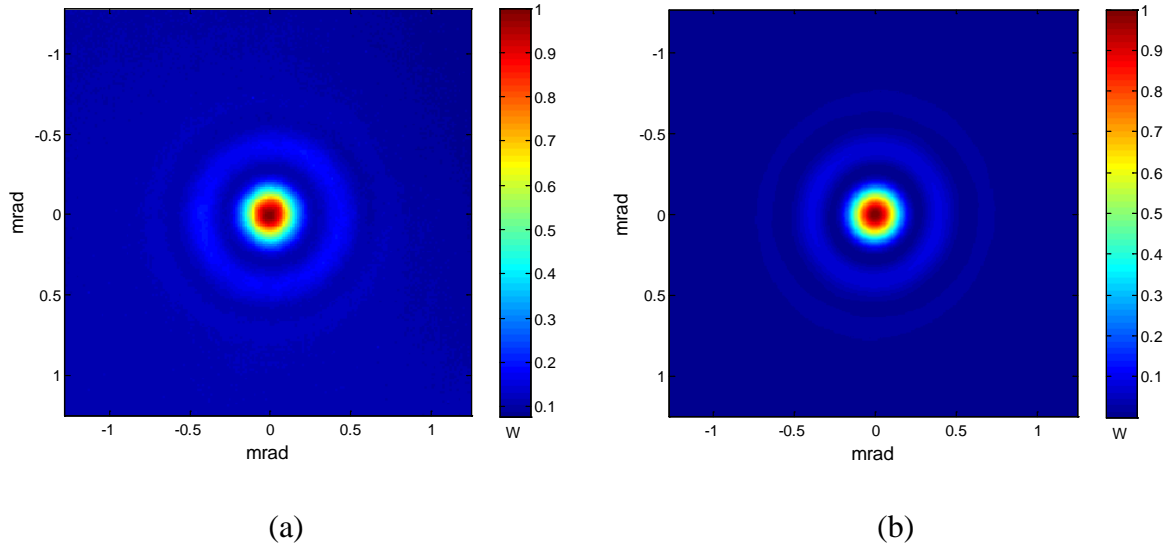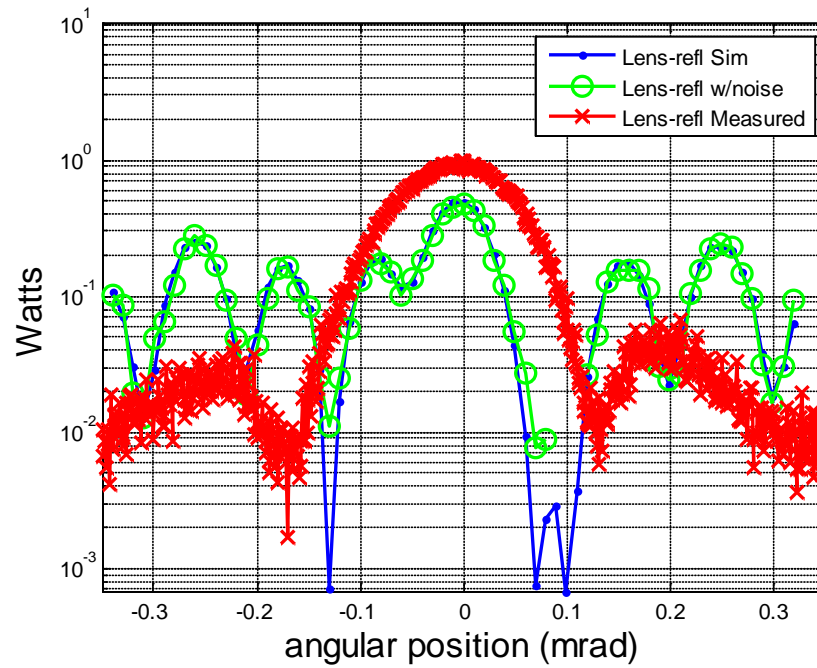

Figure 14. Slice of reflected power distribution from lens-reflector target interrogated at 1064nm. Note the poor agreement between simulations and measurements.

coated mirrors which are highly reflective at both wavelengths. The 4636nm lens was a Thor Labs LA8100 Silicon lens. Figure 15 is the transmission curve for uncoated silicon which shows that wavelengths shorter than 1µm are completely absorbed. This means no source light from the Zygo can pass the lens, so the aberrations measured by the Zygo were completely due to surface reflections from the lens. This is definitely not the target characteristic that was desired to be measured. The 1064nm lens was a Thor Labs AC254-100-B made from LAKN22 and SFL6 glass [37]. This lens was coated for >99% transmission from 650nm to 1050nm and approximately 98% reflectivity at both 632nm and 1064nm. In this case, the Zygo source can pass the lens, but there may be some small front surface reflection that could cause erroneous measured values. The more important effect to consider is the location of the lens focus as a function of wavelength. The AC254-100-B lens is an achromatic doublet, meaning chromatic spherical aberrations have been decreased so the focal point occurs in the same location and maintains focused spot size for the 706.5nm, 855nm, and 1015nm design wavelengths.
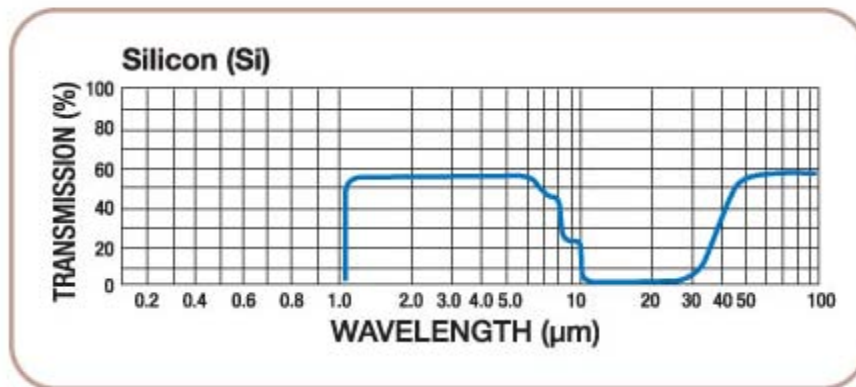
Figure 15. Transmission curve for uncoated Silicon [43]**.**

Figure 16 shows the shift in focal point from 100mm for a specified wavelength.

Comparing the 632nm and 1064nm wavelengths with some interpolation suggests a focal

point difference of approximately 100µm. This corresponds to nearly 94 waves of

defocus between the Zygo measurement at 632nm and the interrogation wavelength of

1064nm. A second important consideration must be made because an achromatic lens is

used in this retro-reflecting target. An achromatic lens corrects for spherical aberration

on the way to the mirror in the target, so if the mirror were set precisely at focus, the

target reflection would not be effected by any aberrations other then the physical

aberrations due to the fabrication of the optics. Since the mirror is not precisely at focus,

the phase curvature of the field incident on the lens prior to exiting the target is different

than the phase curvature expected for a field propagating from focus. Additionally,

achromatic lenses are sensitive to propagation direction and will introduce, rather than
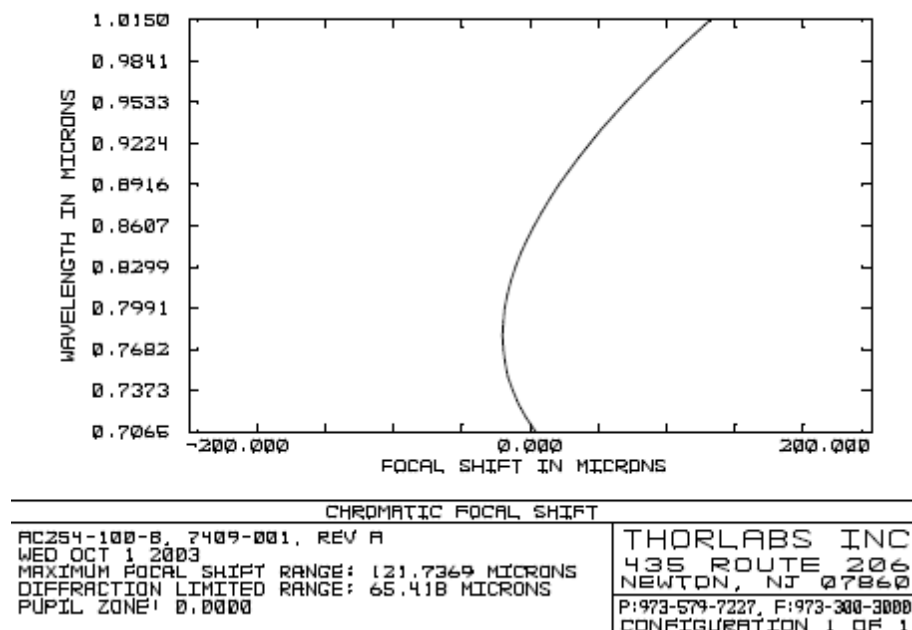
Figure 16. Curve of the focal point position change as a function of wavelength for the 1065nm target lens [37]**.**

correct, for spherical aberration when used in the incorrect orientation [37]. Again, this is a chromatic aberration so the spherical aberration measured with the Zygo will be different than the aberration realized at 1064nm. All these effects combined create a condition for dubious results from the Zygo interferometer for the purposes of this experiment. This is not to say that interferometry would not work to model a complex optical system with focusing elements. If interferometry is to be used, there must be clever accounting for chromatic effects or the interferometer measurements must be made at the same wavelength with which the target will be interrogated.

Modeling the reflected phase front from the lens-reflector target was still possible, despite the interferometry setback, using the simulation and making several important assumptions. Using the simulation, with code incorporated to apply Zernike polynomial aberrations to a target, the aberration coefficients which produced the power distribution measured on the SLCT were used as the new target aberrations. The new coefficients were found with trial and error and some knowledge of the target properties. One such property was the idea that the reflected wavefront was most likely to be dominated by defocus and spherical aberration. The Thor Labs optics used are of high quality and manufactured to high tolerance to minimize aberrations. The geometry of the lens-reflector target inherently introduces defocus and spherical aberration. Placement of the mirror at any position other than focus is equivalent to adding a defocus phase aberration to the reflected phase-front. The lens-reflector targets were assembled using the SLCT by mounting the lens and mirror independently on a rail and translating the mirror until the maximum amount of reflected power was observed on the SLCT camera. The lens and mirror were then fixed into a mounting tube so the lens and mirror could stay at the

53

appropriate distance for the remainder of the experiments. The precision with which the

mirror was able to be placed at the focus of the 100mm lens for both targets was not high

compared to the wavelengths being used. Because of the longer wavelength, the 4636nm

target allows a higher tolerance in placing the lens at focus than is allowed for the

1064nm target [34]. The introduction of spherical aberration occurs for essentially the

same reasons in the 4636nm and 1064nm targets. The 4636nm lens is a plano-convex

singlet. Singlet lenses introduce spherical aberration because they cannot focus all rays

to the exact same point [37]. This, coupled with the limited ability to place the mirror at

precise focus and plano-convex lenses being sensitive to propagation direction introduces

spherical aberration to the reflected field on the reflection path. The achromatic doublet

lens of the 1064nm target introduces spherical aberrations, as explained previously,

because of the presence of defocus in the target and the lens's sensitivity to propagation

direction [37]. Therefore, the approach to find the correct reflection aberrations for the

target will assume defocus and spherical aberrations dominate all others. For both lens

targets, adjusting the sampling suggested by Equations (25), (26), and (27) was necessary

to prevent phase aliasing. The increase in spatial frequency over the target was

significant for both targets and contributed to a loss of resolution over the detector.

Figure 17 shows the reflected phase that, when applied to simulation, produces the

simulated power distribution in the far-field which most closely approximates the

measured power distribution. Note that the phase in radians is much larger for the case of

the 1064nm target, meaning the 1064nm target is much more defocused than the 4636nm

target. Also, the spatial frequency of the mesh plot is much higher for the 1064nm target

since the derivative of the phase is much larger. It was certainly only coincidence that

(a)

(b)
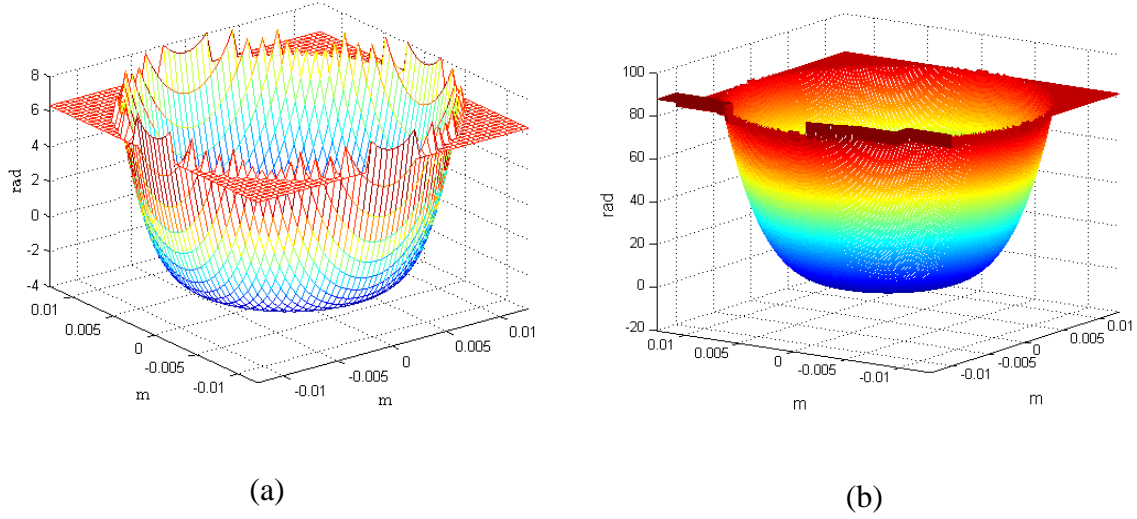
Figure 17. Reflected phase from lens-reflector target estimated using the vacuum simulation to determine defocus and spherical aberration coefficients. (a) 4636nm target (b) 1064nm target. Phase shift effects observed outside of target diameter are due to phase unwrapping algorithm.

the Zygo phase measurements of the 4636nm lens-reflector target were close to the actual

aberrations. Figure 18 and Figure 19 show the same data sets as before, this time for the

4636nm lens-reflector target. Also, Figure 19 shows the deviation of the target from a

one-inch circular flat mirror as a reference.

The new phase of the 1064nm lens-reflector target provided some unique

challenges with respect to the aliasing and resolution constraints as discussed in Chapter

3. The derivative of the reflected phase from the 1064nm lens-reflector target is so large

that the grid spacing required to avoid phase aliasing in the target plane is 90µm, so the

total size of the grid with 512 samples per side is 4.6cm. This grid size is less than twice

the size of the target aperture at 2.54cm. The source that is used in these simulations, as

discussed in Chapter 3 and shown in Figure 2(a), must have a large enough extent so that

the target aperture is uniformly illuminated in the vacuum simulation and the power at the
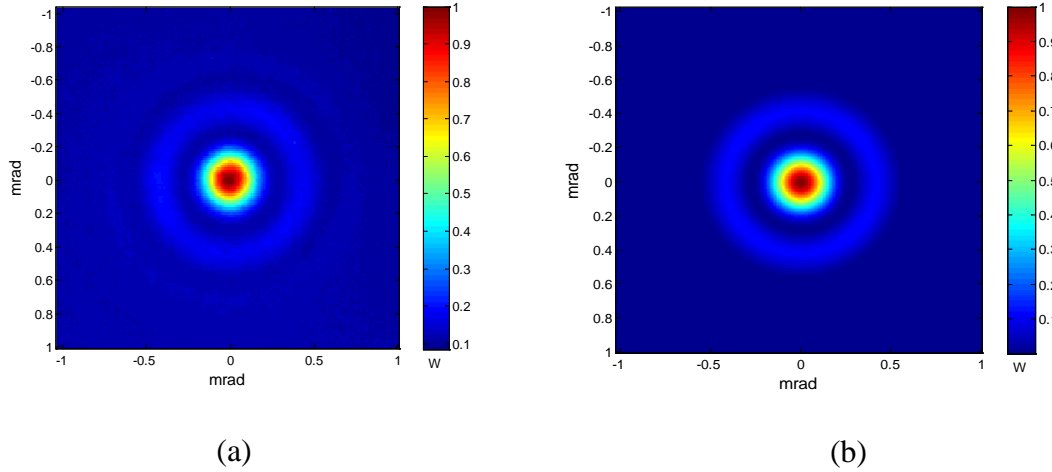
Figure 18. Peak normalized reflected power distributions of the lens-reflector target interrogated at 4636nm with phase aberrations estimated through simulation. (a) SLCT data. (b) Simulated data using receiver plane grid spacing as determined by the target plane grid spacing.
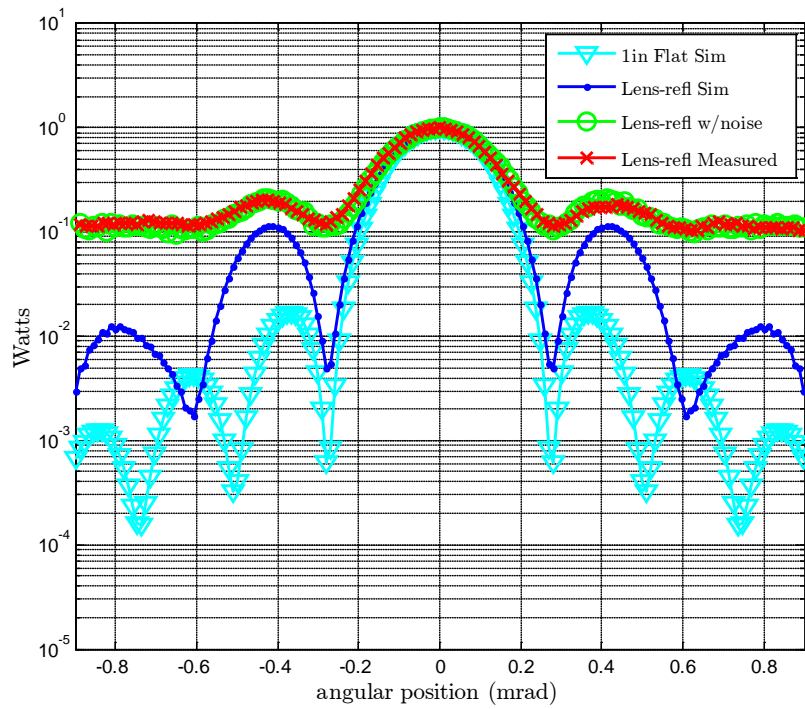
Figure 19. Slice of reflected power distribution from 1in diameter lens-reflector target interrogated at 4636nm with phase aberrations estimated through simulation. Agreement obtained that is even better than that shown with the Zygo determined phase.

target is as expected in the turbulence propagation. Since the 4.6cm grid is not large

enough for the source beam to meet both criteria, a larger target plane grid spacing is

used for the source propagation. In order to multiply the target phase by the source field,

the source field must be down-sampled to the same grid spacing as the target phase. This

is done using bilinear interpolation from the *interp2* function in MATLAB. As a result of

the small grid spacing at the target plane, a large grid spacing is required in the receiver

plane, a requirement made evident by Equations (26) and (27). The required grid spacing

is on the order of the receiver aperture diameter. One pixel is not enough resolution at

the receiver to produce reliable results. To resolve this resolution shortcoming, the field

in the receiver plane is up-sampled using the *interp2* function to a smaller grid spacing

allowing for more pixels across the detector aperture. This method succeeds in

improving resolution over both target and receiver planes for both the vacuum simulation

and the turbulence simulation. Figure 20 shows the two-dimensional reflected power

distribution from the 1064nm lens target in the far-field (2km) for both SLCT

measurements in (a) and simulated results with the simulation-determined phase

aberration in (b). Figure 20(b) shows the results of using the interpolation method as

described above for the distribution in the receiver plane. The agreement is markedly

better. The phase aberrations estimated through simulation were quite large and the

number of samples over the target aperture had to be increased substantially to avoid

phase aliasing. The sampling constraints presented in Chapter 3 require that the grid

spacing in the receiver plane be increased in concert with a reduction in the target plane

grid spacing. In order to get enough resolution over the reflected power distribution to

compare to measured data, the grid size has to be set to a size that is too large to achieve

(a)   (b)
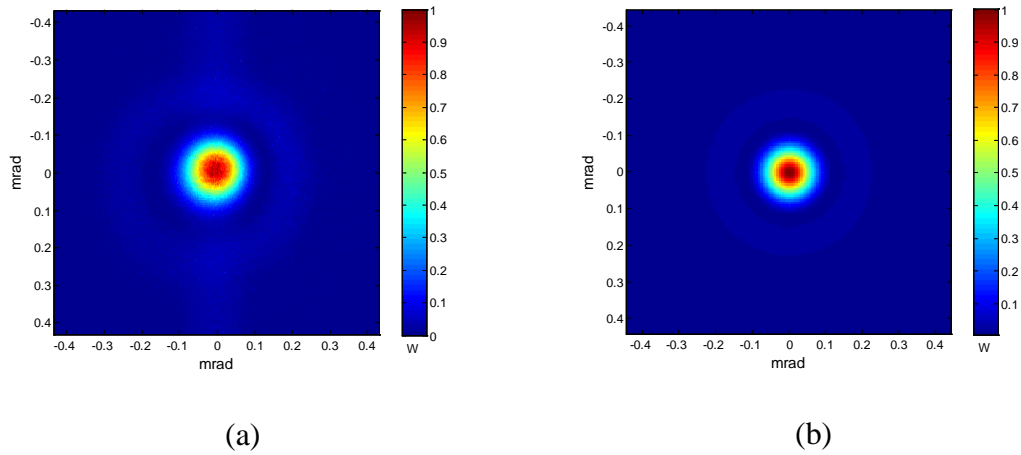
Figure 20. Peak normalized reflected power distributions of the lens-reflector target interrogated at 1064nm with phase aberrations estimated through simulation. (a) SLCT data. (b) Simulated data using interpolation to enhance resolution
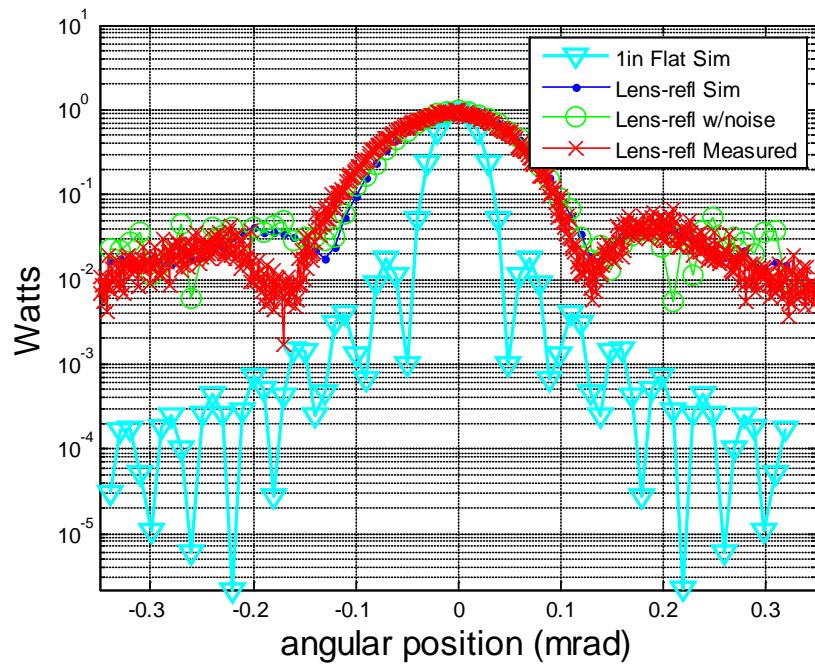
Figure 21. Slice of reflected power distribution from 1in diameter lens-reflector target interrogated at 1064nm with phase aberrations estimated through simulation. Agreement is much higher than using the phase measured by the Zygo interferometer. Agreement between simulation and measured values suffers at angular positions further off-axis because the beam splitter used on the SLCT artificially stretches the power distribution.

58

desired resolution. The interpolation method as demonstrated definitely helps with resolution and was subsequently used as necessary in simulations. Figure 21 shows a slice through the distribution. This time, the agreement between measured and simulation is vastly improved. Because of the large angular extent of this reflected power distribution compared to the other targets, the aberration caused by the beam splitter and camera misalignment at angles smaller then -0.07mrad is more pronounced.

C. Turbulence Simulations

With field data collected by experiment as described in Chapter 3, turbulence simulations were run to compare simulated data to measured data. The simulation was designed to accept input parameters from the experiment. Table 1 lists the input parameters determined by experiment that are loaded into the simulation. This approach allowed for the simulation to make a direct watts-to-watts comparison with measured data. Conversion factors for measured data were developed for the detector fixtures using the SLCT where known laser power and detector irradiance was related to detector voltage. Target reflectivity was obtained through manufacturer specification. Atmospheric transmission was determined with the LEEDR software package developed by the AFIT Center for Directed Energy [39]. Figure 22 shows the flux collected by a one-inch aperture centered at some angular position from the monostatic position. The three curves present are the vacuum simulation results, the field measured results, and the turbulence simulation results. The turbulence curves, like the measurement curves, are a slice of the reflected power distribution. They were generated in simulation by computing the average flux at the receiver after propagation through a path with

Table 1. Experiment parameters for input into simulation.

Experiment Parameter	Value (Units)	Error
Range	782m	±2m
Target aperture diameter	.0254m	negligible
Receiver aperture diameter	.0254m	negligible
Source laser power	Measurement dependent Mean: 893MWIR@1064nm 770MWIR @4636nm	±(6% of measurement+1.03MWIR)
Source laser divergence	4.96mrad @1064nm 3.42mrad @4636nm	±0.1mrad
Source laser spot size	6.10mm @1064nm 4.49mm @4636nm	±0.01mm
Detector position	Start at beam edge 1cm increments @1064nm 2cm increments @4636nm	±0.5mm
$C_n{}^2$	Measurement Dependent	Measurement Dependent
Detector voltage	Measurement Dependent	±0.01mV
Detector voltage to watts conversion factor	6.11×10^{-5}W/V @1064nm 9.37×10^{-6}W/V @4636nm	$\pm 1.44 \times 10^{-5}$ $\pm 3.91 \times 10^{-7}$
Atmospheric transmission	96.9% @1064nm 96.3% @4636nm	negligible
Corner cube reflectivity (net)	88.47% @1064nm 94.12% @4636nm	± 2% of reflectivity
Lens-reflector reflectivity of optics (net)	94.12% @1064nm 95.08% @4636nm	± 2% of reflectivity

corresponding path averaged C_n^2. To elaborate, each field measurement has an associated

path averaged C_n^2 as reported by the scintillometer. To find the power distribution

corresponding to one measurement, a propagation was executed through 50 random

draws of a turbulence path with the turbulence path C_n^2 corresponding to the

measurement. Instead of averaging the 50 propagations together, an averaging scheme
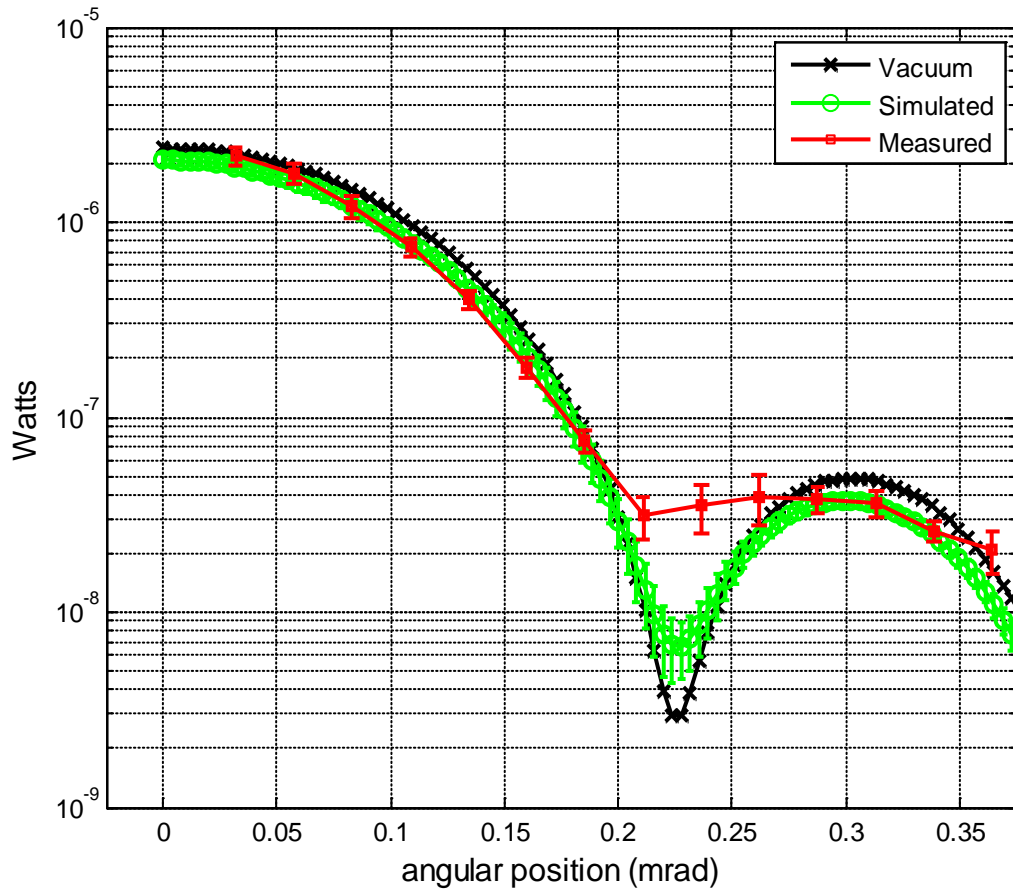
Figure 22. Bistatic power distribution from the corner cube target interrogated at 4636nm. Simulated propagations in turbulence and vacuum (Simulated and Vacuum on legend) are compared with field measurements (Measured on legend).

more closely aligned with the field measurement process was adopted. Measured values

were taken with the lock-in amplifier reporting power with a 3sec time average so that

the average measured power values as reported are an average of long-term power

fluctuations. Therefore, it is appropriate to collect a set of short-term simulations, take

the average of small sets of short-term values yielding a set of long-term values, then

average the long-term values together. Because of computational time considerations, 50

propagations were conducted for each detector position (more propagations are always better). The power distributions from those 50 propagations were split up into sets of ten and averaged to obtain a set of ten long term values. The ten long term values were then averaged to yield the mean power received and the standard deviation of the long term fluctuations were computed. The received flux for the average distribution was calculated by centering a one-inch aperture at each pixel in a horizontal slice of the average reflected power distribution. This process was repeated for each C_n^2 value. Once the off-axis flux was measured from each turbulent path, the values were averaged, yielding the average simulated distribution in turbulence curve, as shown. The error bars shown on simulated power in turbulence values correspond to long term fluctuations within 2σ of the mean as computed in simulation so that 95% of the fluctuations fall within those bounds. The average measured values from experiment are shown with error. The error is the sum of the 2σ field measurement fluctuations and the measurement error as computed with errors given in Table 1. The simulation is considered validated by the experiment if the error bars of the simulated power distribution overlap with the error of the experimental measurement. Figure 22 does not meet this criteria in some regions (most notably in the nulls and side lobes). It is proposed that this deviation was directly related to the setup of the field experiment which resulted in an unaccounted loss of source coherence.

In general, atmospheric turbulence causes a loss of spatial coherence to a propagating spatially coherent field (while it is not accurate to say the laser source is perfectly coherent, it is treated as one in simulation since the actual laser source coherence properties are unknown and are likely negligible compared to the effects of

turbulence propagation). Goodman shows the effects of spatial coherence loss on a circular diffracting aperture where the peak is attenuated and power is redistributed off-axis resulting in a blurring of the fringes [40]. Figure 23 is a photograph of the source/receiver bench setup inside a heated trailer at the test range. The area of interest is the trailer door where the source exits and the target reflection is detected. Turbulence theory shows that C_n^2 is proportional to the time average magnitude squared fluctuations in temperature between two points[4]. Since the trailer atmosphere was warmer than the
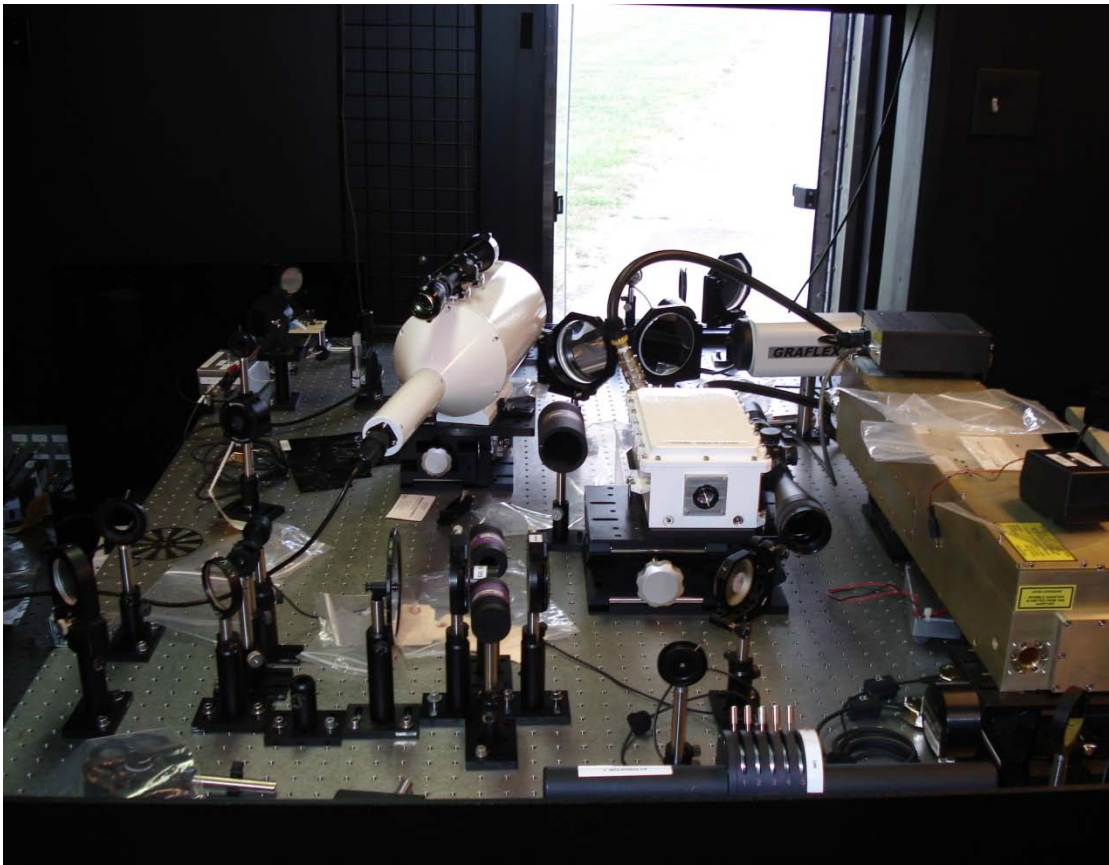
Figure 23. Photograph of field experiment setup. Note the door giving the source beam access to the range. It is at this door where the warm air from the trailer and the cold air of the atmosphere outside mixed and caused a visible turbulence layer that was not measurable by the scintillometer receiver (also shown in the picture).

atmosphere outside the trailer, a turbulence boundary layer was set up directly in the turbulence path. While temperature measurements were not taken on site during testing, historical WPAFB weather data can be accessed at www.weatherunderground.com. Field measurements were taken from November 19-21, 2008 where the ambient temperatures outside at measurement times ranged from 28° to 37° F. The trailer was heated to approximately 65° F. This was a substantial temperature gradient resulting in a thin strong turbulence layer immediately at the door. It is well understood that strong turbulence layers have very small inner scales [4]. The small inner scale translates to the presence of aberrations of high spatial frequency in the turbulence layer. Therefore, the source beam, which is much smaller in diameter than the received target reflection, would be susceptible to the door turbulence layer. One attempt to capture the effects of the door turbulence on the experiment was to move the scintillometer receiver from outside to inside the trailer. This was a futile attempt, however, because the scintillometer is not designed to capture short turbulence paths, especially when close to the aperture. The scintillometer aperture is large enough that small scale turbulence effects over a short path close to the aperture do not significantly contribute to measured irradiance fluctuations and the computed C_n^2. Accounting for the turbulence layer at the door in simulation was accomplished through consideration of the physics and some trial and error. The most successful modeling technique was to introduce a single random Kolmogorov phase screen with the Fried parameter (see Equation (23)) set to a value which achieved desired results. The layer is very thin compared to the entire path distance and does not appear to contribute to scintillation of the transmitted or received signals in most cases so the single phase screen model is reasonable. The placement of

64

the phase screen at the target was driven by necessity as it would have been more desirable to place the screen at the source where the physical turbulence layer was located. In simulation, the source beam (as discussed in Chapter 3) was modeled as a point source which is only several pixels in extent in the source plane. Essentially, the source plane lacks the resolution to apply a phase screen and achieve physical effects and does not account for the divergence of the beam through the door turbulence layer. Placing the screen at the target allows for sufficient resolution over the target and effectively simulates the small scale wavefront aberrations from the door turbulence layer that have propagated with the source to the target plane. The Fried parameter of the phase screen was chosen entirely by trial and error. Since the 782m path average Fried parameter was hundreds of millimeters, it was certain that the value of the screen used must be smaller. After multiple simulations, the Fried parameter chosen for the random Kolmogorov phase screen used was 0.07m and 0.04m for the 4636nm interrogations and the 1064nm interrogations, respectively. The Fried parameters have different values for different wavelengths because the field measurements were taken on different days with different temperature differences. Ideally, some characterization of the door turbulence layer would have been done to account for its effects, i.e. the C_n^2 value of the layer, the volume of the layer, and the identification of the appropriate turbulence power spectrum. This would have been a non-trivial characterization beyond the scope of this work. Future experiments performed in similar conditions should attempt execution at ambient temperatures.

Although the simulation solution to the door turbulence layer is not physically precise, it certainly demonstrates the effects of the turbulence layer and provides some

correction to the results. Figure 24 shows the same bistatic simulated and field measurement curves as Figure 22 but with correction for the door turbulence layer with the single phase screen at the target method. The door correction does increase the simulated power at the 0.25mrad null as was observed in the field measurements and expected by the loss of source coherence. However, the door turbulence correction also takes the simulated power out of range of the measurement error for some other points
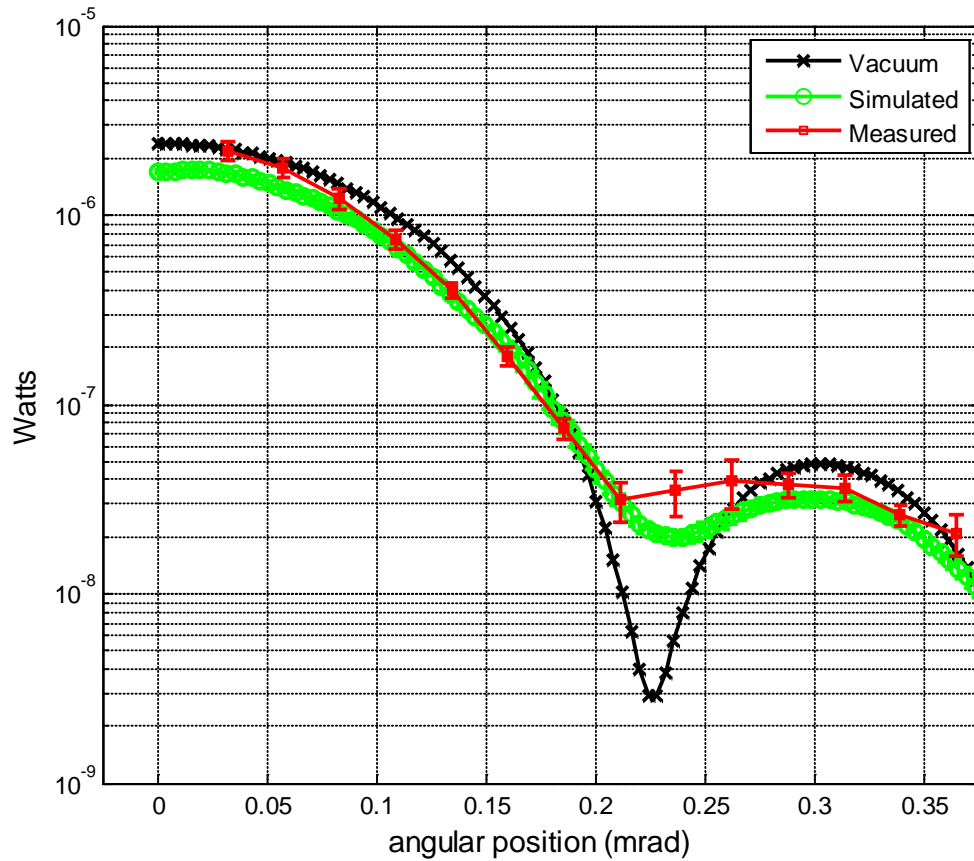
Figure 24. Bistatic power distribution from the corner cube target interrogated at 4636nm corrected for the turbulence layer at the source/receiver. Simulated propagations in turbulence and vacuum (Simulated and Vacuum on legend) are compared with field measurements (Measured on legend).

66

that were previously estimated well. This is due directly to having to guess at the door

turbulence layer model, and illustrates the importance of complete characterization of the

propagation path. Never the less, the simulation does quite well at predicting the

reflected power at most detector positions for the corner cube target interrogated at

4636nm.

Figure 25 shows the same simulation and field measurement comparison but for

the corner cube target interrogated at 1064nm. Shorter wavelengths are more susceptible
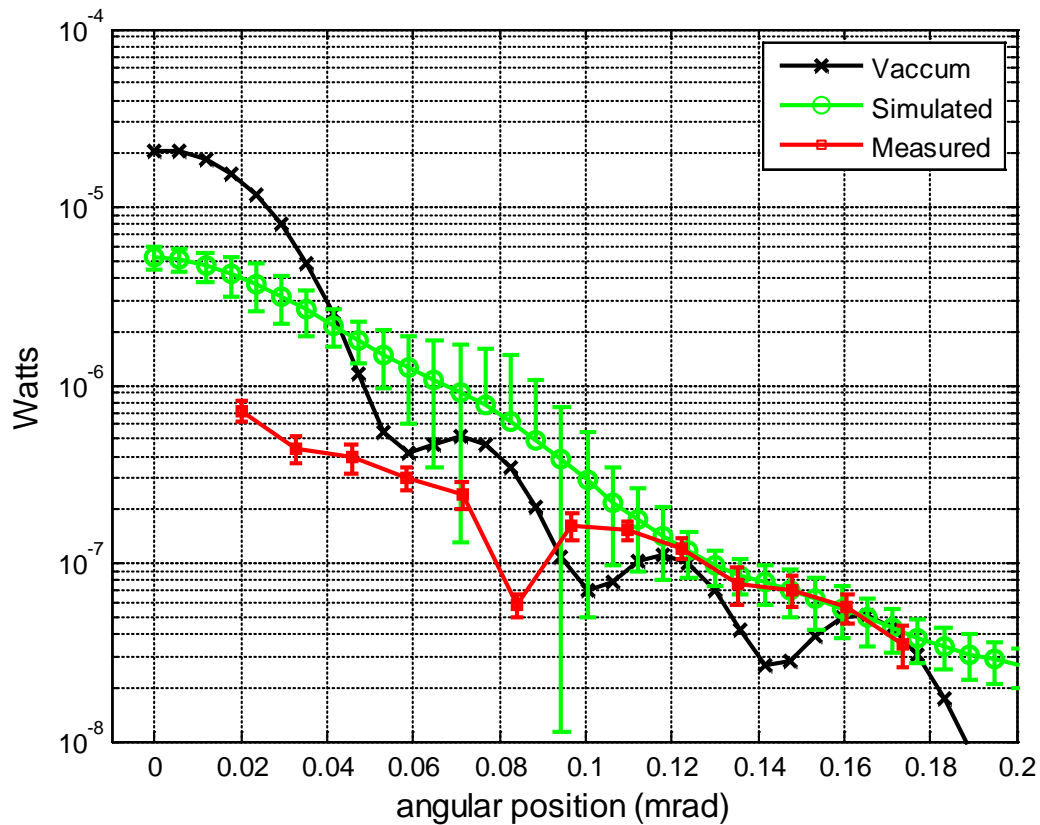
Figure 25. Bistatic power distribution from the corner cube target interrogated at 1064nm. Simulated propagations in turbulence and vacuum (Simulated and Vacuum on legend) are compared with field measurements (Measured on legend).

to turbulence and target aberrations when compared to longer wavelengths. This effect is definitely noted in the 1064nm interrogation when compared to the 4636 nm interrogation of the same target. Figure 25 demonstrates how the turbulence eliminates nearly all of the vacuum propagation's diffraction structure. It does appear, however, that there is an anomalous field measurement at the 0.085mrad detector position since it does not correspond well with the total field measurement set or the simulations, but it does correspond to a large standard deviation in the mean as shown in Figure 25 . The effects of the door turbulence layer are quite pronounced in Figure 25, manifesting in different observed slopes of the turbulence simulation and field measurement curve. Consistent with the anticipated effects of the door turbulence layer, measured values show more power redistributed from positions close to on-axis out to the side lobes of the pattern than is predicted by simulation using only the path average C_n^2. Figure 26 shows the results after application of the door turbulence correction phase screen. While the correction is not perfect, the corrected turbulence simulation curve approaches the approximate angular slope of the field measurement curve and the simulation predicts return power within error.

Figure 27, Figure 28, Figure 29, and Figure 30 show the same plots as shown for the corner cube target but for the lens-reflector targets with the estimated target reflection phase, not the Zygo measured phase. The observations about the results made for previous targets are essentially the same. The 4636nm lens-reflector target shows nearly all data points are predicted within error after correction although the two closest to the on axis position do not. A final observation about the door turbulence is that there is

68
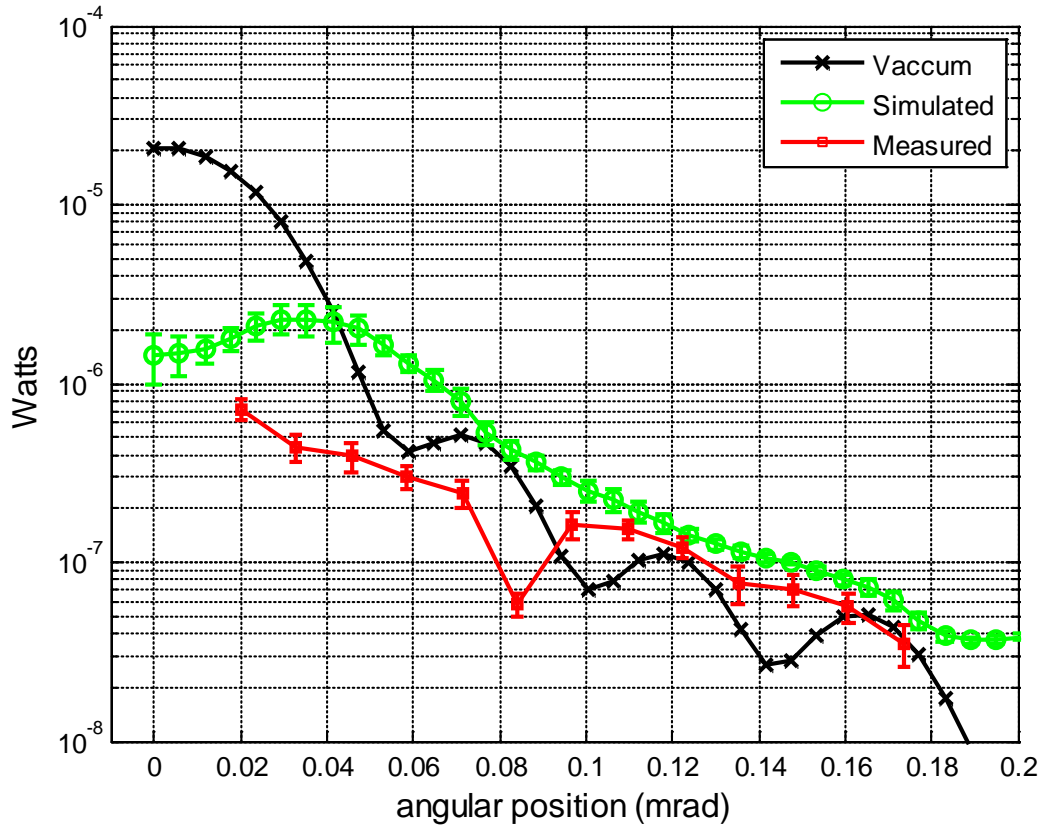
Figure 26. Bistatic power distribution from the corner cube target interrogated at 1064nm corrected for the turbulence layer at the source/receiver. Simulated propagations in turbulence and vacuum (Simulated and Vacuum on legend) are compared with field measurements (Measured on legend).

likely a scintillation component to the layer that was initially presumed to be small. The

door correction does appear to correct for the general shape or angular slope of the

distribution, but (specifically in the case of the 1064nm targets) there appears to be a

constant offset between power values predicted by simulation with door turbulence

correction and the measured values. Adding several phase screens at the receiver plane

with some propagation distance between them t o simulate the volume of the propagation

layer may have added the scintillation needed to scale the magnitude of the simulated

distribution. Again, guessing at the turbulence path correction makes it difficult to

Figure 27. Bistatic power distribution from the lens-reflector target interrogated at 4636nm. Simulated propagations in turbulence and vacuum (Simulated and Vacuum on legend) are compared with field measurements (Measured on legend).
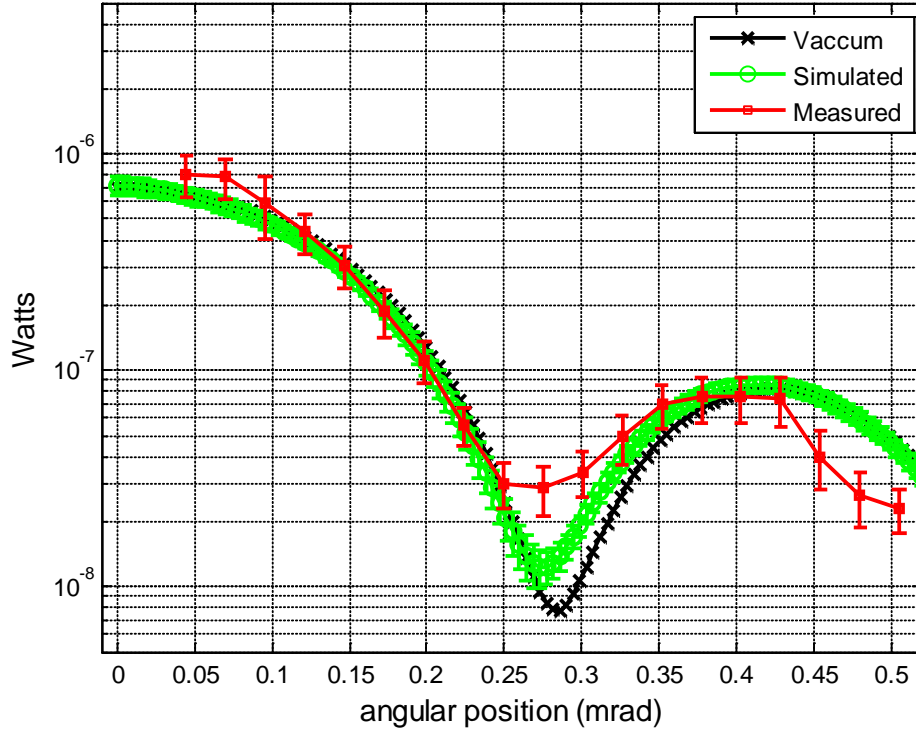
produce an exact match between simulated and measured received power, especially for

shorter wavelengths where precise characterization of the propagation path is critical. All

results considered, the consistency of the trends between simulated and measured data

and the ability of the simulation to predict many measured data points within error is

encouraging.

D. Summary

Laboratory experiments have shown the validity of using wave optics and phase

aberrations to predict the reflected power distribution from an OA target. The three
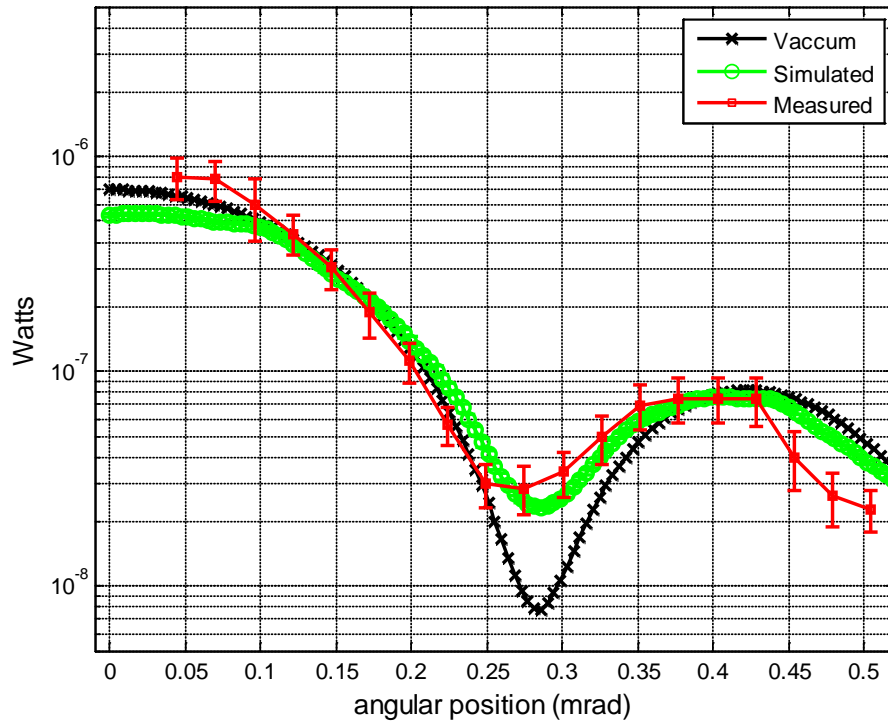
Figure 28. Bistatic power distribution from the lens-reflector target interrogated at 4636nm corrected for the turbulence layer at the source/receiver. Simulated propagations in turbulence and vacuum (Simulated and Vacuum on legend) are compared with field measurements (Measured on legend).

primary areas that could have improved results were improving the observed dynamic

range of the FPA detector images, capturing target irradiance so the measured reflected

power could be computed and compared with simulated power, and the ability to do

chromatic interferometry or another more direct method of measuring the actual reflected

phase aberrations from the lens-reflector targets. After comparison of simulated and field

measured data, it has been shown that a wave optics simulation that incorporates the

correct experimental variables and path dynamics of an OA laser interrogation system

could predict returned power within the accuracy of the measurement. The critical

variable that limited the conclusions that can be drawn from the data presented here is

71
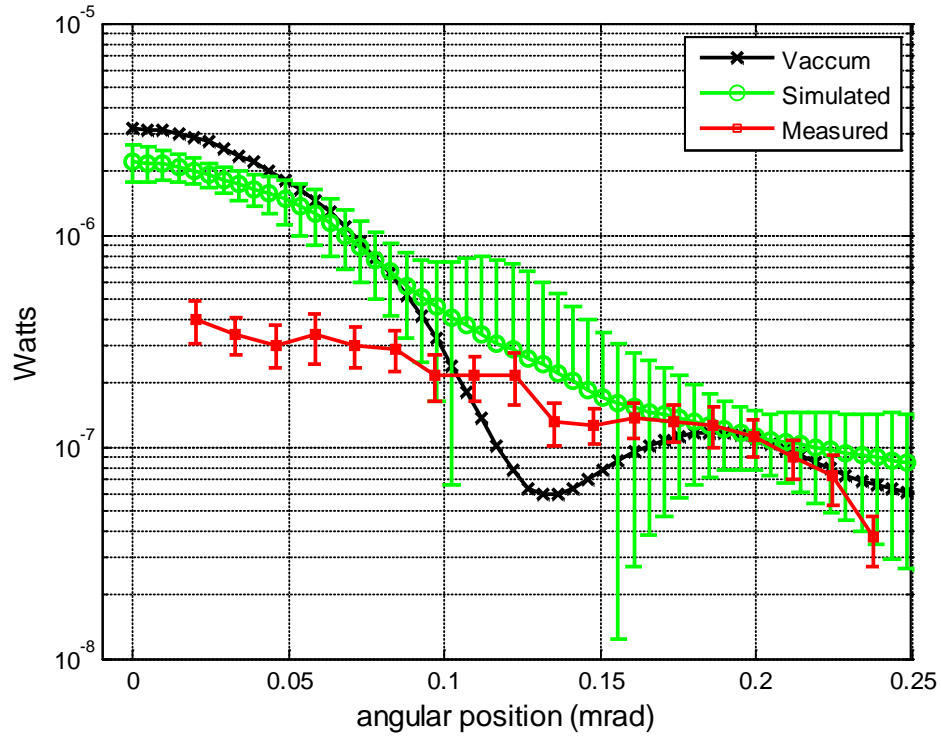
Figure 29. Bistatic power distribution from the lens-reflector target interrogated at 1064nm. Simulated propagations in turbulence and vacuum (Simulated and Vacuum on legend) are compared with field measurements (Measured on legend).

propagation path characterization. Although it was shown that a larger than expected loss of source coherence was definitely a result of the door turbulence layer, additional unaccounted for effects are clearly present in the field measured received power distributions when compared with door-corrected simulated measurements. Never the less, the trends observed from attempting to correct for the incomplete characterization of turbulence are quite promising and the reflected power distributions for the targets interrogated at 4636nm demonstrate that power at most receiver positions can be accurately predicted.
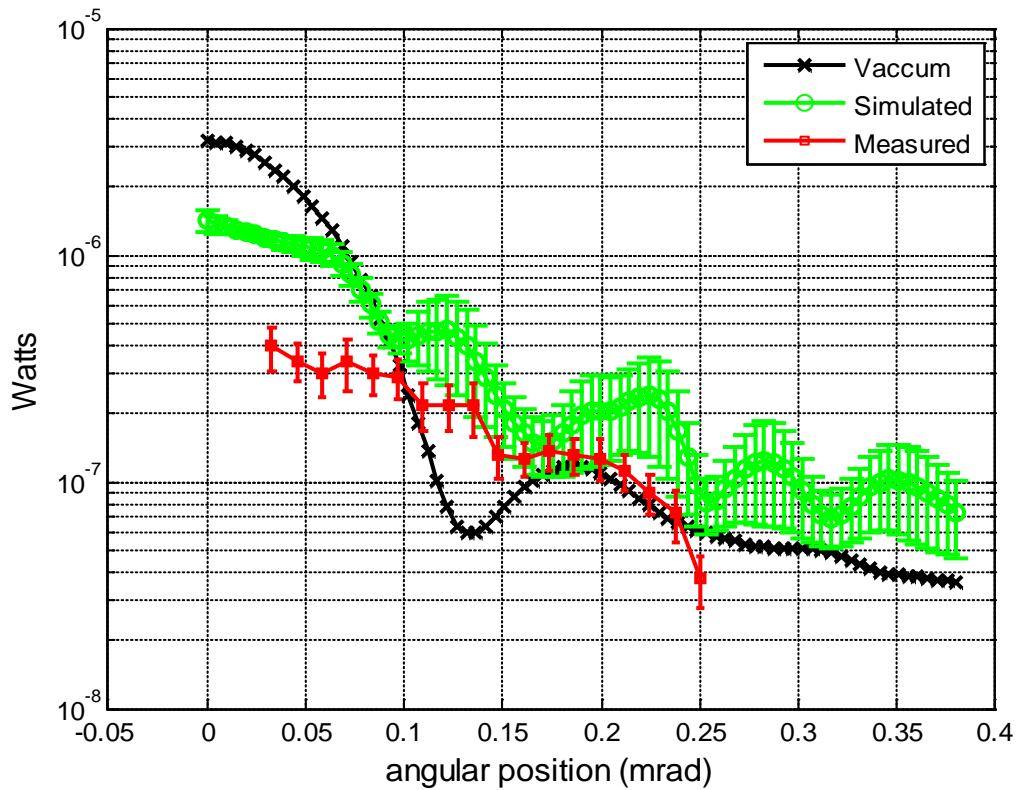
Figure 30. Bistatic power distribution from the lens-reflector target interrogated at 1064nm corrected for the turbulence layer at the source/receiver. Simulated propagations in turbulence and vacuum (Simulated and Vacuum on legend) are compared with field measurements (Measured on legend). Having to guess at the turbulence level of the door makes it difficult to find an exact match of simulation with data, but the simulated distribution appears to over-predict power only by a constant offset.

V. Conclusions and Recommendations

A. Chapter Overview

The research methodology and results as presented in this thesis constitute a proof of concept utilizing numeric wave optics simulations to predict returned power from OA targets. The research has shown that there are important considerations that must be made when designing a simulation, to include source, target, receiver, and path characteristics and dynamics. There are practical implications for the results presented but there is a significant amount of research and engineering necessary to develop and apply simulations to an OA characterization system.

B. Conclusions of Research

The results presented in this research have shown that numeric wave optics can be used to develop a simulation which provides reflected power distributions from retroreflecting targets in the presence of atmospheric turbulence. Utilizing both field and laboratory experiments of reflected power distributions, a numeric wave optics simulation was designed which predicts within error those power distributions for a specified target, where the error is due to measurement uncertainty and random fluctuations due to atmospheric turbulence. Despite non-ideal path characterization, the simulation was able to predict returned power for many bistatic receiver positions in the presence of turbulence for both a simple corner cube reflector and a more complex OA target with a focusing element at two different wavelengths; the simulation methods presented and applied are sound.

74

There are several important practical considerations for proper implementation of a wave optics simulation like the one presented. One of the most constraining aspects of the simulation was minimizing aliasing in magnitude and phase while maintaining spatial frequencies high enough in the target and receiver plane for acceptable resolution. The number of samples in a plane was constrained by computation time. With the exception of the corner cube target interrogated at 1064nm, all simulations were run with grids using 2^9 samples per side. The longest target simulations involved 19 measurement positions with corresponding C_n^2. Each position received 50 independent propagations per position with ten phase screens over the path. For 19 detector positions, that is a total of 950, 10-step propagations taking six hours or more to run to completion, running MATLAB on a standard desktop computer with a 3.6GHz processor and 2GByte RAM. Efficiency was not specifically considered while writing the code, but the computational load is high regardless due to all the Fourier transforms necessary. Limited by the number of samples in the grid, the lens-reflector targets which had phase aberrations with large derivatives required a high spatial frequency. The high spatial frequency at the target plane caused a less-than-ideal, but functional, spatial frequency in the receiver plane. Interpolation to up-sample/down-sample to increase/decrease resolution in special cases proved to be a viable solution to resolution problems in tightly constrained scenarios. For any laser interrogation scenario of interest, the size of the detector and receiver apertures, target phase aberrations, interrogation range, and the interrogation wavelength determine sampling and resolution constraints, should be carefully modeled or represented in simulation.

As is true with any model, the ability of the simulation to predict field results was strongly dependent on the input parameters. Because of the relatively long time constant of 3 seconds used to take field measurements, power fluctuations due to turbulence were much less of a contributor to the error present in measured values (as shown in the Chapter 4 results) than the error introduced by measurement of input parameters. It would have been interesting to observe measured power fluctuations on a time scale on the order of the laser pulse frequency. This would have allowed for the collection of scintillation statistics in the field as a function of C_n^2 which could have been matched to scintillation statistics in simulation. Future experiments interested in such information should use electronic data collection to make a faster sampling rate practical.

Although modeling targets for simulation was done adequately in this research to achieve desired results, an accurate and efficient method of direct measurement was not demonstrated. Using reflected phase aberrations is clearly a viable solution. Interferometery is likely to be a good method for measuring the reflected phase for input into simulation but it has some practical limitations and is rather expensive. It was shown that use of the Zygo interferometer is impractical for targets with focusing elements due to its single-wavelength interrogation. A wavefront sensor integrated into the SLCT would be a reasonable solution which would work with the interrogation wavelength of choice. If the reflected phasefront is expected to be dominated by only a few aberrations, like the lens-reflector targets used here, guessing at the aberration coefficients to achieve measured results may be good enough. More complex optical systems would likely require a more robust solution, perhaps one which uses nonlinear optimization to find the correct coefficients. The SLCT proved effective in providing far-field images of a

target's reflected power, without which the vacuum simulation could not have been validated and the phase of the lens-reflector target reflection could not have been determined.

In terms of target characterization, if the appropriate OCS is known for a target under a specific laser interrogation geometry, Equation (1) can be used to predict returned power in vacuum in the same way the wave optics simulation presented does. In addition to computing the peak DOCS of targets, the SLCT images could be used to compute different DOCS and TOCS values of targets, both monostatic and bistatic, given the laser interrogation geometry. In order to do this effectively, care must be taken when characterizing the cameras on the SLCT so that noise and dynamic range are adequate to make measurements of interest. Image background subtraction, non-uniformity correction, and variable integration times could be used in concert to capture high fidelity images for OCS computation. Accounting for the angular resolution of a bistatic detector is an important practical limitation when applying a bistatic OCS computed on the SLCT, as described in Chapter 3.

As was demonstrated by the turbulence layer present at the door of the trailer, characterization of the propagation path in field measurements is very important to achieving accurate results. To model more realistic systems, additional modeling of the propagation path and system dynamics will be necessary. For example, a mobile fieldable system could introduce aero-optical turbulence effects and mechanical vibration. Many of these effects are wavelength-dependent where shorter wavelengths will be more susceptible to variations in the propagation path.

C. Recommendations for Future Research

The work presented in this thesis is primarily a proof of concept that numeric wave optics can be used to predict returned power from an OA target in the presence of turbulence. The chief task of using a wave optics simulation to detect and identify practical OA targets remains. Similar experiments and simulations as conducted here should be performed for some real OA targets/threats to identify challenges in simulating more complex optical systems. All targets were interrogated at boresight, a condition that is not likely to be met in a practical scenario, so aspect angle of targets should be considered. In addition, real OA targets are likely to have an OCS that is much smaller than the optical targets used in this research and real laser interrogation systems will be scanning systems minimizing the total irradiance incident on a target. Probability of detection at various ranges, laser powers, scan rates, and aspect angles will have to be computed for some real targets.

The idea of target identification from laser radar signatures is not new [40,41]. Target identification algorithms typically rely on matching unique features of a target to a known signature. With information on the retroreflected power distribution for a target of interest, perhaps enough unique features exist to make target identification possible. Results presented in this research clearly demonstrate that even relatively similar targets can have unique reflected power distributions. The effects of turbulence, specifically the loss of source coherence, could be an important consideration in the target identification problem. Shapiro showed that the reflectance of objects can change when illuminated by light at various levels of coherence [42].

The further research suggested certainly makes use of more field measurements to be matched with simulation results. Field data collection is a lengthy process, and as mentioned in the previous section, is wrought with measurement error. In order to efficiently perform field experiments, it would be very useful to have a specified design for a laser interrogation system which maximizes performance and minimizes errors. Also, digital data collection is critical to understanding scintillation statistics of received power and needs to be implemented if detection measurements are made for a scanning system.

D. Concluding Remarks

The research presented in this thesis has presented a viable solution to predicting reflected power from an OA target while providing information about the way that power is distributed. This is a valuable, albeit small, piece to solving the larger problem of target identification from a tactical system. Hopefully, future researchers will continue to advance towards solving that larger problem with the aid of the research presented here.

Appendix A

A. Laser Sources (same for laboratory and field measurements)

a. **4636nm Laser Source:** Coherent doubled CO_2 MID-IR-2 laser, pulsed or quasi-

CW

b. **1064nm Source:** Crystalaser, Nd:YAG laser, CW (chopped for modulation)

B. Cameras and Detectors

a. **NIR Camera on SLCT: Cohu** 7712 (1M Pixel, 7.4µmX7.4µm resolution). All

images taken with the Cohu 7712 were background subtracted post-processing as

described in Chapter 4, Section B and non-uniformity corrected (NUC). NUC

was accomplished by taking measurements of a white light source in a diffuse

sphere for 12 different irradiance levels, computing the average count per pixel at

each irradiance level, and applying a gain to each pixel.

b. **MWIR Camera:** Custom L3 Comm/Cincinnati Electronics, 256X256 pixel

camera, 30µmX30µm pixels, liquid nitrogen cooled
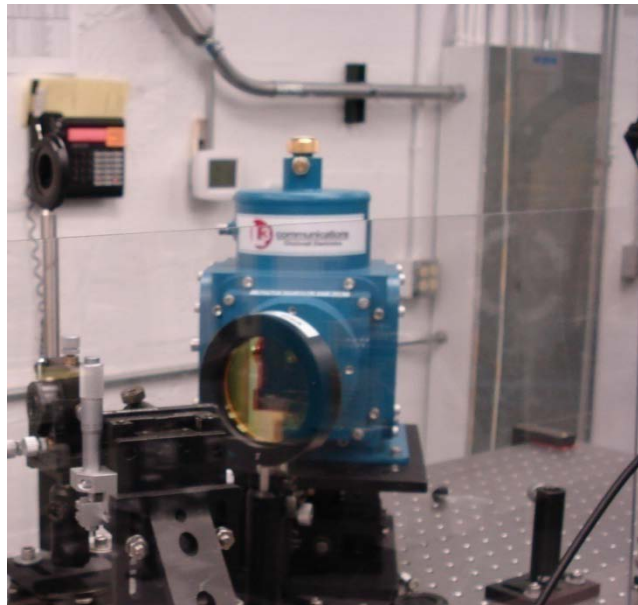
c. **NIR Detector:** ThorLabs PDA400, switchable Gain, Amplified InGaAs

Detector. 1mm single element detector. Set to 10dB of gain
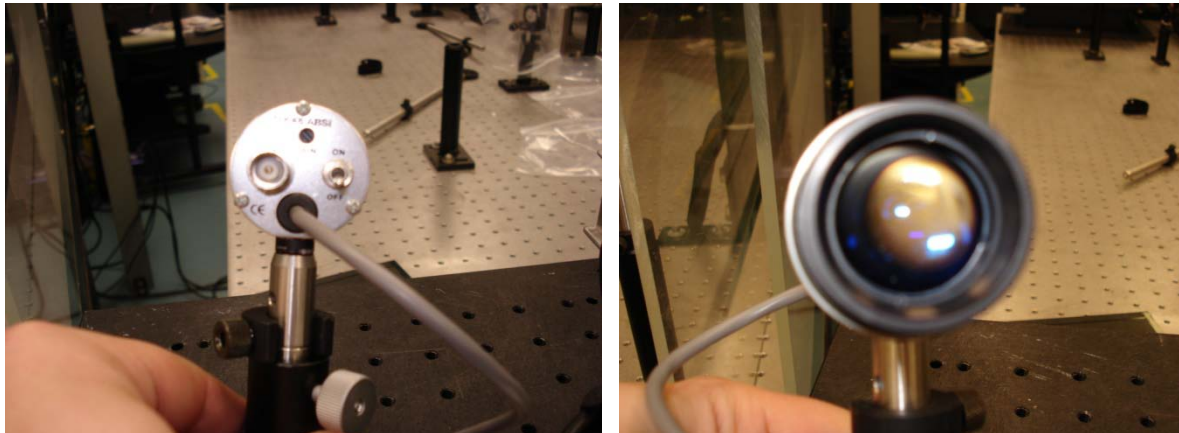
d. **NIR Detector Collection Lens:** ThorLabs LA1951-B, Plano-Convex,

Diam=0.0254m, f=0.0254m

AR coating reflectivity for Thor Labs lenses:
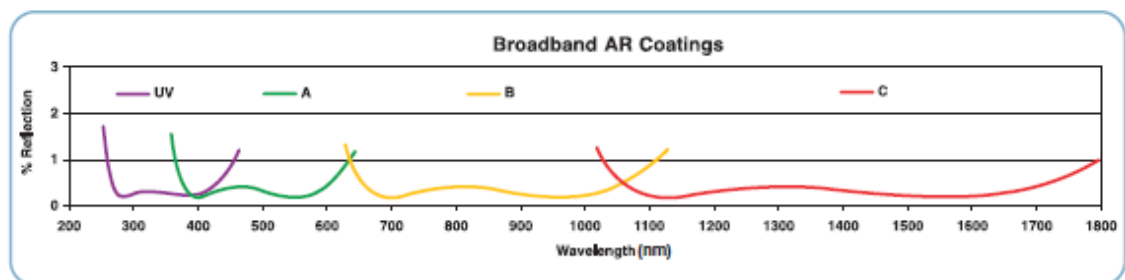
e. MWIR Detector: Cincinnati Electronics SDD-32EO-S1, powered InSb 1mm

single element detector, liquid nitrogen cooled.
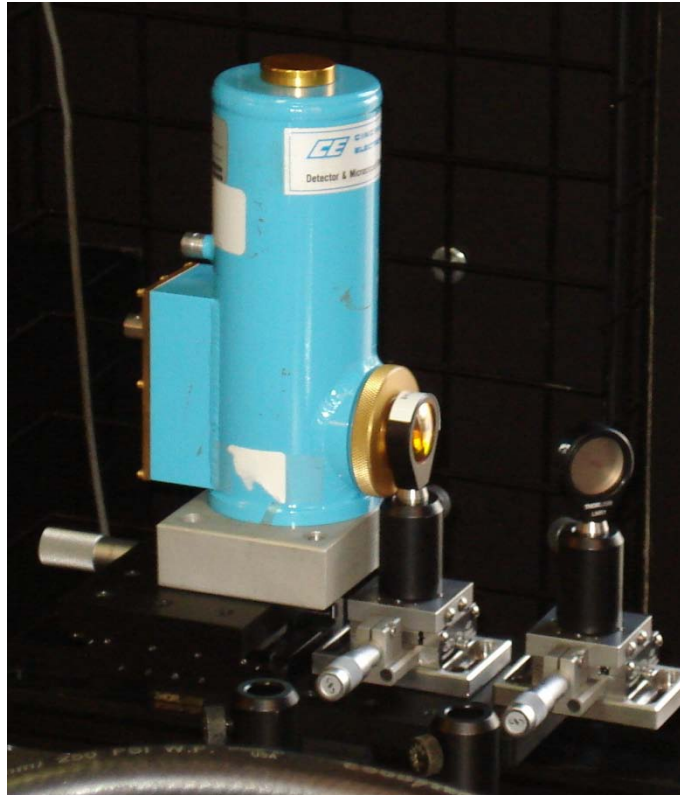
f. MWIR Detector Collection Lens: ISP Optics ZC-PM-25-25, Zinc Selenide

CVD Positive meniscus lens, Diam=0.0254m, f=0.0254m, Anti-reflection (AR)

coated for 3µm-12µm

Diameter tolerance	+0,-0.005" (+0,-0.13 mm)
Center Thickness tolerance	+/-0.008" (+/-0.2 mm)
Design Wavelength	10.6 microns
Focal Length Tolerance	+/-2%
Surface Quality	60/40
Clear Aperture	90% Central Diameter
Wedge Angle	<3 arc min
Surface Irregularity	1/20 λ at 10.6 microns

g. MWIR Detector Collection Mirror: ThorLabs PF10-03-P01, Protected silver mirror, Diam=0.0254m
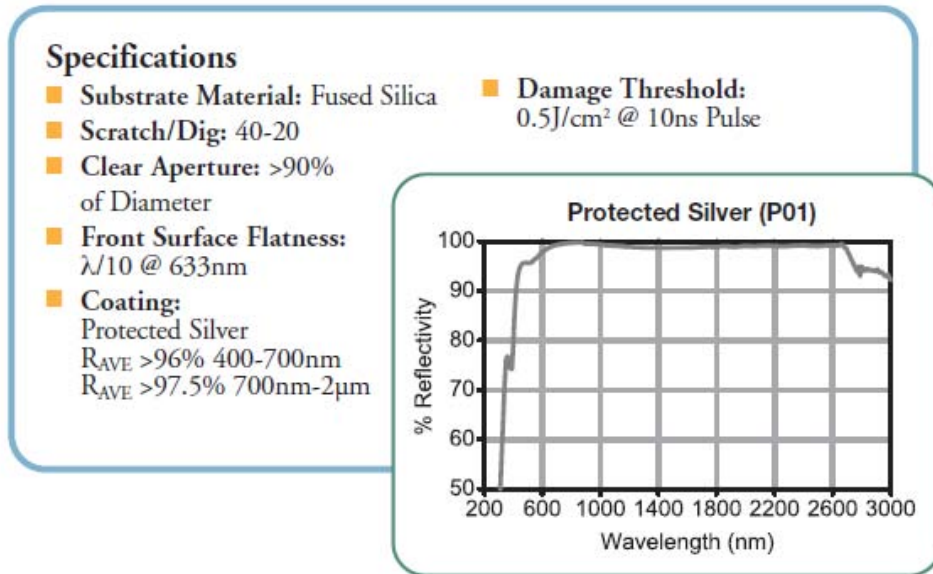
C. Targets

a. Corner Cube: PLX Inc Omni Wave Hollow Reflector, used for both 1064nm and 4636nm interrogations, protected gold coated

Drawing callouts:
- ø1.0clr.apt.
- 1 3/4
- ø2.00
- 90° ø1 5/8
- 1/4
- 1/2
- 1 3/4
- 1 15/16
- drill thru ø0.29 (4)-typ.@90°
- M6x1 by 5/16"dp.
- #1/4-20NC thd. by 5/16"dp.-typ.
- 45°

REVISIONS

REV	DESCRIPTION	DATE	BY
B	dimensions added	10/15/98	ISH
C	redesigned forP/N1026;P/N changed	6/22/99	ISH

POS	QTY REQD	CODE IDENT	PART OR IDENTIFYING NO	NOMENCLATURE OR DESCRIPTION	MATERIAL SPECIFICATION
				PARTS LIST	

PLX
40 WEST JEFRYN BLVD.
DEER PARK, NY 11729

UNLESS OTHERWISE SPECIFIED DIMENSIONS ARE IN INCHES TOLERANCES ARE:

FRACTIONS DECIMALS ANGLES
±1/16" ± XX .030" ± 1°
± XXX .010"

	APPROVAL	DATE
DRAWN	ISH	6/19/98
CHECKED		6/22/99
ISSUED		

MATERIAL

FINISH

1026CHG

APPLICATION   DO NOT SCALE DRAWING

ø1.0" CLEAR APERTURE
OMNI WAVE HOLLOW RETROREFLECTOR
MAIN ASSEMBLY LAYOUT

SIZE	STD	DWG.NO.	REV.
A		OW-10	C
SCALE 1:1		SHEET 1OF1	

Angle = 55 Degree(s)   % REFL   Unpol.   S-Pol.   P-Pol.

PROTECTED GOLD

b. Lens-Reflector Targets

1   1064nm Target:

(1) Lens: ThorLabs AC-254-100-B, Material: LAKN22-SFL6, Acromatic-doublet, AR coated with B coating, Diam=0.0254m, focl=0.1m

Specifications

- **Design Wavelengths:** 706.5, 855, and 1015nm
- **Diameter Tolerance:** +0.00/-0.10mm
- **Focal Length Tolerance:** ±1%
- **Scratch-Dig:** 40-20
- **Centration:** ≤3arcmin
- **Clear Aperture:** >90% of Dia.
- **Coating:** Ravg <0.5% From 650-1050nm (B Coating Range)
- **Operating Temperature:** -40°C to +85°C

(2) Mirror: ThorLabs PF10-03-P01, Protected silver mirror, Diam=0.0254m

2   1064nm Target:

(1) Lens: Thor Labs LA8100, Silicon plano-convex, Diam=0.0254m, focl=0.1m

Material	Silicon
Design Wavelength	4.0 µm
Wavelength Range	1.2 - 8.0 µm
Index of Refraction	3.425 at Design Wavelength
Coating*	BBAR 98% from 3 - 5 µm
Centration	≤ 3 arcmin
Clear Aperture	>80% of Diameter
Focal Length Tolerance	±1%
Surface Quality	40/20 Scratch Dig
Diameter	1" (25.4 mm)
Diameter Tolerance	+0.00 mm / -0.10 mm

(2) Mirror: ThorLabs PF10-03-P01, Protected silver mirror, Diam=0.0254m

D. Other Equipment

a. Lock-in-amplifier: Stanford Research Systems SR830 DSP lock-in

Settings	4636nm and 1064nm
Time Constant	3sec @ 12dB
Coupling	AC
Input	Line+2X line filters
Phase	Positive edge
Frequency	100kHz
Noise mode	Low

b. Detector Preamplifier: Stanford Research Systems SR560 Low Noise

preamplifier

Settings	4636nm	1064nm
Gain	5 V/V	20 V/V
Coupling	AC	AC
Gain Mode	Low Noise	Low Noise
Filter Cutoffs	6dB/octave @ 1kHz	6dB/octave @ 10Hz

c. **Radiometer:** Laser Precision Corp RK-5710, used for measuring target irradiance and detector calibration in laboratory and field

SPECIFICATIONS

Spectral response	0.2 - 20.0 μm
Maximum total power	10 W
Maximum average power density	100 W/cm^2
Noise equivalent power	100 nW
Calibration accuracy	±5%
Linearity	±0.5%
Detector active area dimensions	11.3 mm (1.0 cm^2)
Full scale ranges	6; 200 (300) μW - 10 W (instrument dependent)
Probe dimensions (l x w x h)	17.0 cm x 9.0 cm x 5.0 cm (6.7" x 3.6" x 2.0")
Probe and chopper (l x w x h)	19.0 cm x 9.0 cm x 10.5 cm (7.5" x 3.6" x 4.2")
Probe weight	0.7 kg (1.5 lb)
Probe and chopper weight	1.6 kg (3.5 lb)

d. Scintillometer: BLS-900

Receiver

Transmitter

Transmitter Specifications

Specifications	BLS450	BLS900
Main radiation source	444 LEDs GaAlAs	888 GaAlAs LEDs
Degradation time MTTF	55 000 hours	55 000 hours
Auxiliary radiation source	18 LEDs visible	36 LEDs
Maximal optical power	7.5 W	15 W
Wavelength	880 nm	880 nm
Beam Divergence	16°	16°
Pulse Repetition Rates (PRR)	1Hz, 5Hz, 25 Hz, 125Hz	1Hz, 5Hz, 25 Hz, 125Hz
Pulse length	8 ms	8 ms
Modulation frequency	1750 Hz	1750 Hz and 2500 Hz
Operation voltage	12 VDC	12 VDC
Power consumption	40 W 8 W 2 W 1 W	80 W 16 W 4 W 1 W
Dimensions	180 x 180 x 135 mm	364 x 180 x 135 mm
Weight	4.5 kg	8.5 kg

Receiver Specifications

Specifications	BLS450 and BLS900
Lens Focal length Diameter Field of view	Plan convex 450 mm 145 mm 8 mrad
Detectors Sensitive area Sensitive area	2 Si Photodiodes 15 mm² 5 mm²
Dimension	Ø160 x 590 mm
Weight	7.6 kg

Processing unit specifications

90

Specifications	BLS450, BLS900, BLS2000
Integration time	1 min
Data Storage Capacity	Approx. 2 years
Internal clock	Date and time
Operation temperature range	-20°C ~ + 50°C
Operation voltage	12 VDC
Weight	4.7 kg
Dimension	230 x 200 x 180 mm
Power consumption (including Receiver)	15 W
Power consumption BLS2000 Heating	9.6 W

e. **Power Meter:** Coherent FieldMaster GS with LM-10HTD detector head, 20sec

integration time. Used to determine laser source power in field.

f. Beam Camera: Spiricon, Inc. Pyrocam III. Used to measure source beam spot size and divergence in field.

Application	IR and UV
Spectral response	157 - 355nm 1.06 - 3000μm
Interchangeable windows	See selection in Ordering Information section
Active area	12.4mm x 12.4mm
Element spacing	100μm x 100μm
Number of elements	124 x 124
Chopped CW Operation	
Chopping frequencies (Optional chopper)	24Hz 48Hz
Sensitivity (RMS noise limit)	220 nW/pixel (24Hz) 320 nW/pixel (48Hz) 2.2 mW/cm² (24Hz) 3.2 mW/cm² (48Hz)
Noise equivalent power (NEP)	45 nW/Hz$^{1/2}$/pixel (1Hz)
Saturation power	2.2W/cm² (24Hz) 3.2W/cm² (48Hz)
Damage total power Over entire array Power density	 2W 8W/cm²
Pulsed Operation	
Laser pulse rate	Single-shot to 1000Hz
Pulse width	1fs - 12.8ms
Sensitivity (peak noise limit)	7nJ/pixel 70μJ/cm²

g. Zygo Interferometer
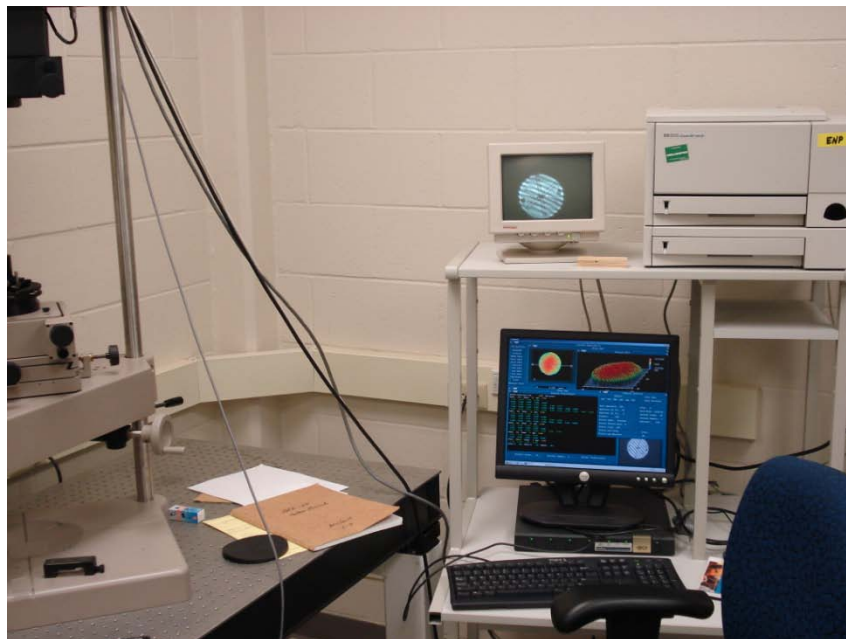
SYSTEM

Measurement Technique	Laser-based visual interferometry
Measurement Capability	Measure form and flatness characteristics of super finished, highly reflective surfaces and optics
Test Beam Diameter Options	4 inch: 4 in. (102 mm) 6 inch: 6 in. (152 mm)
Configuration Options	Horizontal Vertical, 3-rod, downward looking Vertical, 3-rod, upward looking
Optical Centerline	4.25 in. (108 mm)
Alignment System	Quick Fringe Acquisition System (QFAS) with twin spot reticle
Alignment Field of View	4 inch: ±3 degrees 6 inch: ±2 degrees
Focus	Fixed, ±1 m depth of field
Part Viewing	9-inch monitor
Video Output	525 lines/60 Hz (2:1 interlace) RS-170, or 625 lines/60 Hz
System Quality (1)	Plano testing: $\lambda/20$ Spherical testing: $\lambda/10$

LASER SPECIFICATIONS

Type	Helium-Neon, Class II
Wavelength	632.8 nm
Output Power at Aperture	≤ 1 milliwatt
Beam Polarization	Circular
Coherence Length	Greater than 328 ft (100 m)

MetroPro Software used with Zernike application

E. Simulation

    a.   Software

        1   Matlab 7.4.0 R2007b

        2   WaveProp, Ver. 1.07, The Optical Sciences Company

        3   AOTools, Ver. 1.3, The Optical Sciences Company

    b. Hardware

        1 Dell Precision 670

        2   Intel Xenon 3.60GHz CPU

        3   2.00 GBytes RAM

Bibliography

[1] Nathan J. Able, "Effects of Aberrations on Optical Cross Section Measurements," 2004.

[2] Jade M. Lemery, "Electro-Optic Sensor Detection Via Optically Augmented Retroreflections," WPAFB, 2006.

[3] W. P. Cole, "Atmospheric-Turbulence-Effects Correction Factors for the Laser Range Equation," WPAFB, 2008.

[4] Larry C Andrews and Ronald L Phillips, *Laser Beam Propagation through Random Media*, 2nd ed. Bellingham, WA: SPIE, 2005.

[5] M C Roggemann and B Welsh, *Imaging Through Turbulence*.: CRC Press, 1996.

[6] James A Dowling and Peter M Livingston, "Behavior of focused beams in atmospheric turbulence: Measurements and comments on the theory," *J. Opt. Soc. Am. A*, pp. 846-858, 1973.

[7] R F Lutomirski and H T Yura, "Propagation of a Finite Optical Beam in an Inhomogeneous Medium," *Applied Optics*, pp. 1652-1658, 1971.

[8] R R Parenti and R J Sasiela, "Distribution Models for Optical Scintillation Due to Atmospheric Turbulence," Lexington, Tech Report 2005.

[9] Italo Toselli, Larry C Andrews, Ronald L Phillips, and Valter Ferrero, "Scintillation index of optical plane wave propagating through non Kolmogorov moderate-strong turbulence," in *Optics in Atmospheric Propagation and Adaptive Systems X*, 2007, pp. 67470B1-12.

[10] Rod Frehlich, "Simulation of laser propagation in a turbulent atmosphere," *Applied Optics*, pp. 393-397, 2000.

[11] G Gbur and O Korotkova, "Angular Specturm Representation for the Propagation of Arbitrary Coherent and Partially Coherent Beams Through Atmospheric Turbulence," *J. Opt. Soc. Am. A*, vol. 24, no. 3, pp. 745-752, March 2007.

[12] G Gimmestad, R David, J Stewart, J Wood, and M Dawsey, "LIDAR Technique for Range Profiles of Turbulence," Georgia Tech Research Institute, Atlanta, Tech Report 2005.

[13] R F Lutomirski and R E Warren, "Atmospheric Distortions in a Retroreflected Laser Signal," *Applied Optics*, pp. 840-846, 1975.

[14] Feng Zengfang and Yuezhong Song, "Beam Spread Induced by Atmospheric Turbulence in a Folded Path," *Journal of Optics*, pp. 1-11, 1997.

[15] J. Fred Holmes, "Enhancement of backscattered intensity for a bistatic lidar operating in atmospheric turbulence," *Applied Optics*, pp. 2643-2646, 1991.

[16] L C Andrews, R L Phillips, and W B Miller, "Mutual coherence function for a double-passage retroreflected optical wave in atmospheric turbulence," *Applied Optics*, pp. 698-708, 1997.

[17] L Lading, S Hanson, and A Skov Jensen, "Diffraction-limited lidars: the impact of refractive turbulence," *Applied Optics*, vol. 23, no. 15, pp. 2492-2497, 1984.

[18] Jim F. Riker, "Validation of Active Tracking Laser Beam Propagation and Target Signature Predictions," in *Laser Weapons Technology III*, 2002, pp. 45-56.

[19] S Chandler, G Lukesh, and C Barnard, "Estimation of Satellite Laser Optical Cross Section: A Comparison of Simuations and Field Results," in *Proceedings of SPIE*, vol. 4167, 2001, pp. 53-63.

[20] W. Gamble, "Standard Optical Augmentation Measurement Methodology," 1986.

[21] John. Arenberg, "Optical Cross Section Primer," 1989.

[22] Wolf and Zissis, *The Infrared Handbook*.: Environmental Institute of Michigan, 1978.

[23] Walter P Cole, M A Marciniak, and M B Haeri, "Modification of the Laser Range Equation," , 2008.

[24] Walter P Cole, M A Marciniak, S C Cain, J E McCrae, and M B Haeri, "Laser Illumination of Optical Devices," , 2008.

[25] Walter P Cole, M A Marciniak, and M B Haeri, "Atmospheric-Turbulence-Effects Correction Factors for the Laser Range Equation," vol. 47, 2008.

[26] P Chiu, I Shih, S Shi, and P Laou, "Study of laser reflection of infrared cameras with germanium optics," in *Targets and Backgrounds IX: Characterization and Representation*, 2003, pp. 190-199.

[27] E L Dereniak and G D Borman, *Infrared Detectors and Systems*.: Wiley-Interscience, 1996.

[28] Joseph W. Goodman, *Fourier Optics*, 3rd ed. Englewood, CA: Roberts & Company, 2005.

[29] J. D. Schmidt, Class Notes, May 2008.

[30] Vladimir P Lukin and Boris V Fortes, *Adaptive Beaming and Imaging in the Turbulent Atmosphere*. Bellingham: SPIE, 2002.

[31] Nathan Blaunstien and Christos Christodoulou, *Radio Propagation and Adaptive Antennas for Wireless Communication Links*. Hoboken, NJ: John Wiley and Sons, Inc., 2007.

[32] A V Oppenheim, R W Schafer, and J R Buck, *Discrete-Time Signal Processing*, 2nd ed. Upper Saddle River, New Jersey: Prentice-Hall, 1999.

[33] T J Brennan, P H Roberts, and D C Zimmerman, WaveProp: A Wave Optics Simulation System for Use With MATLAB Users Guide, 2008, Version 1.07.

[34] Daniel Malacara, *Optical Shop Testing*, 3rd ed. Hoboken, New Jersey: John Wiley and Sons Inc, 2007.

[35] Max Born and Emil Wolf, *Principles of Optics*, 7th ed. Cambridge, MA: Cambridge University Press, 1999.

[36] Zygo Corporation, *GPI-XP Interferometer System Operation Manual*. Middlefield, MA, 1999.

[37] Thor Labs. (2008, November) Thor Labs. [Online]. http://www.thorlabs.com/NewGroupPage11.cfm?ObjectGroup_ID=259

[38] Thor Labs. (2008, September) Thor Labs Web Site. [Online]. http://www.thorlabs.com/NewGroupPage9.cfm?ObjectGroup_ID=1779

[39] S T Fiorino et al., "The HELEEOS Atmospheric Effects Package: A Probabilistic Method for Evaluating Uncertainty in Low-Altitude High Energy Laser Effectiveness," *Journal Directed Energy*, pp. pp. 1-13, 2006.

[40] J. W. Goodman, *Statistical Optics*. New York: John Wiley and Sons, Inc., 1985.

[41] I. A. Nepogodina, "Criteria and a method for estimating the information content of the attributes of objects in tasks of laser detection and ranging," *Journal of Optical Technology*, pp. 43-51, 2007.

[42] Jerome I. Glaser, "Some Results in the Bistatic Radar Cross Section (RCS) of Complex Objects," in *Proceedings of the IEEE*, 1989, pp. 639-648.

[43] J. H. Shapiro, "Target-reflectivity theory for coherent laser radarx," *Applied Optics*, vol. 21, no. 18, pp. 3398-3407, 1982.

REPORT DOCUMENTATION PAGE

Form Approved
OMB No. 074-0188

The public reporting burden for this collection of information is estimated to average 1 hour per response, including the time for reviewing instructions, searching existing data sources, gathering and maintaining the data needed, and completing and reviewing the collection of information. Send comments regarding this burden estimate or any other aspect of the collection of information, including suggestions for reducing this burden to Department of Defense, Washington Headquarters Services, Directorate for Information Operations and Reports (0704-0188), 1215 Jefferson Davis Highway, Suite 1204, Arlington, VA 22202-4302. Respondents should be aware that notwithstanding any other provision of law, no person shall be subject to an penalty for failing to comply with a collection of information if it does not display a currently valid OMB control number.
PLEASE DO NOT RETURN YOUR FORM TO THE ABOVE ADDRESS.

1. REPORT DATE *(DD-MM-YYYY)*	2. REPORT TYPE	3. DATES COVERED *(From – To)*
26-03-2009	Master's Thesis	June 2007 – March 2009

4. TITLE AND SUBTITLE	5a. CONTRACT NUMBER
Wave Optics Simulation of Optically Augmented Retroreflections for Monostatic/Bistatic Detection	Proposal 2007-155, JON# 09-130
	5b. GRANT NUMBER
	5c. PROGRAM ELEMENT NUMBER

6. AUTHOR(S)	5d. PROJECT NUMBER
Tatar, John J., Captain, USAF	5e. TASK NUMBER
	5f. WORK UNIT NUMBER

7. PERFORMING ORGANIZATION NAMES(S) AND ADDRESS(S)	8. PERFORMING ORGANIZATION REPORT NUMBER
Air Force Institute of Technology Graduate School of Engineering and Management (AFIT/EN) 2950 Hobson Way, Building 640 WPAFB OH 45433-8865	AFIT/GEO/ENP/09-M03

9. SPONSORING/MONITORING AGENCY NAME(S) AND ADDRESS(ES)	10. SPONSOR/MONITOR'S ACRONYM(S) AFRL/RXPJA
Mr. Anthony Cain, DAF Air Force Research Laboratory (AFMC) Materials and Manufacturing Directorate (AFRL/RX) Survivability and Sensors Materials Division (AFRL/RXPJA) 3005 Hobson Way, Building 71A WPAFB OH 45433-8865	11. SPONSOR/MONITOR'S REPORT NUMBER(S)

12. DISTRIBUTION/AVAILABILITY STATEMENT

APPROVED FOR PUBLIC RELEASE; DISTRIBUTION UNLIMITED.

13. SUPPLEMENTARY NOTES

14. ABSTRACT
Optical devices interrogated with a laser in the appropriate band can exhibit strong, deterministic reflections of the incident beam. This characteristic could be exploited for optical target detection and identification. The distribution of reflected power is strongly dependent on the geometry of the interrogation scenario, atmospheric conditions, and the cross section of the target optical device. Previous work on laser interrogation systems in this area has focused on analytic models or testing. To the best of my knowledge, I am presenting for the first time an approach to predict reflected power for a variety of interrogation configurations, targets, and propagation conditions using numeric simulation based on wave optics. Numeric simulation has a cost advantage over laboratory and field experiments and avoids the limiting complexity of analytic models. Moreover, results demonstrate that reflected power can be predicted within error with an appropriately characterized . Simulations were prepared in MATLAB and run for interrogation scenarios using a simple retro-reflector (corner cube) and a surrogate complex optical system (lens-mirror) target. Laboratory and field experiments were conducted for simulation validation in the absence and presence of atmospheric turbulence with a focus on bistatic receiver configurations. Two interrogation wavelengths, 1064nm and 4636nm, were used. Targets used in this experiment were modeled in simulation by measuring or estimating their deviation from a perfectly flat reflector and applying the corresponding Zernike mode phase aberrations to the simulated pupil. Strengths and limitations of the simulation environment are addressed.

15. SUBJECT TERMS
Optical Augmentation (OA), Laser Radar (Lidar), Infrared Detection, Wave Optics, Atmospheric Turbulence, Light Propagation, Numeric Simulation

16. SECURITY CLASSIFICATION OF:			17. LIMITATION OF ABSTRACT	18. NUMBER OF PAGES	19a. NAME OF RESPONSIBLE PERSON
a. REPORT	b. ABSTRACT	c. THIS PAGE			Michael Marciniak, PhD, AFIT/ENP
					19b. TELEPHONE NUMBER *(Include area code)*
U	U	U	UU	112	(937) 255-6565, ext 4529 (Michael.marciniak@afit.edu)

Standard Form 298 (Rev. 8-98)
Prescribed by ANSI Std. Z39-18